Applied Thermal Engineering 234 (2023) 121319

Contents lists available at ScienceDirect

Applied Thermal Engineering

journal homepage: www.elsevier.com/locate/apthermeng

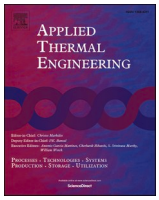

An improved latent heat thermal energy storage using two layers of metal foams

Mohammad Ghalambaz [a,*], Mehdi Fteiti [b], Obai Younis [c,d], Mikhail Sheremet [a], Hiba A. Hasan [e]

[a] Laboratory on Convective Heat and Mass Transfer, Tomsk State University, Tomsk, Russia
[b] Physics Department, Faculty of Applied Science, Umm Al-Qura University, Makkah 24381, Saudi Arabia
[c] Department of Mechanical Engineering, College of Engineering in Wadi Addwasir, Prince Sattam Bin Abdulaziz University, Saudi Arabia
[d] Department of Mechanical Engineering, Faculty of Engineering, University of Khartoum, Khartoum 11111, Sudan
[e] Mechanical Engineering Department, University of Technology, Baghdad, Iraq

ARTICLE INFO

Keywords:
Metal foam layers
Foam configurations
Latent heat thermal energy storage
Melting heat transfer

ABSTRACT

Latent Heat Thermal Energy Storage (LHTES) systems are essential due to their remarkable ability to compactly store significant thermal energy. Their pivotal role extends to various energy applications, prominently including solar heaters and waste thermal energy recovery initiatives. Metal foams have the ability to improve heat transmission and thermal charging of energy storage units dramatically. However, the metal foam cannot store latent heat energy, so the goal is to improve heat transfer by using minimal foam mass. Here, the LHTES is made of several parallel channel enclosures with a square cross-section of 120 mm in height/width. There is a 21 °C temperature difference between the heated channel walls and PCM fusion temperature. In the current study, the influence of the configuration of two metal foam layers was addressed on melting time in LHTES. The idea is to use heavy foam (porosity 0.90) in places where there is low convection and light foams (porosity 0.975) in places with good convection heat transfer to enhance thermal charging and keep the storage weight low. Therefore, three configurations of splitting into half, an L shape division, and splitting diagonally for foam layers were examined. The influence of metal foam configurations on melting volume fraction, thermal energy storage, isotherms, and streamlines was examined. The geometrical configuration of foam layers could significantly influence the thermal charging time and energy storage profiles. The best layer configuration was a horizontal splitting of the enclosure with a light foam layer (high porosity metal foam) at the top. The well-configured foam layer could complete the charging process in 837 s, 32% faster than the same splitting but placing the light foam layer at the bottom.

1. Introduction

Energy is becoming a critical issue for scientists and governments worldwide, owing to the environmental threats posed by fossil fuel pollution and their non-renewable nature. Many efforts have been made to make alternative energy sources and pollution-free energy sources such as solar available to resolve ecological concerns and adjust energy supply and demand. The supply volatility caused by adverse weather and the regular day-night cycle is a significant barrier to the use of solar energy. As a result, recommended techniques that aim to improve the efficiency of existing sources focus on energy-saving technology. Thermal energy storage (TES) is an essential technology increasing energy storage density and has the potential to alleviate energy scarcity [1]. TES can be used as an energy storage system to smooth out supply fluctuations by storing excess thermal energy gathered during daylight hours for later use during dark hours.

As TES methodologies, thermochemical energy, sensible heat, and latent heat have been presented [2–4]. Using phase change material (PCM), latent heat thermal energy storage (LHTES), has vastly greater energy efficiency compared to other solutions; along with their greater storage capacity, PCMs are capable of storing and releasing a substantial amount of energy during melting and solidification [5]. Potential applications of the TES system include energy savings in buildings [6], industrial waste heat recovery [7], solar energy use [8], air-conditioning systems [9], and thermal control of electronic components [10]. Numerous studies on the charging and discharging capabilities of LHTES

* Corresponding author.
E-mail address: m.ghalambaz@gmail.com (M. Ghalambaz).

https://doi.org/10.1016/j.applthermaleng.2023.121319
Received 25 June 2022; Received in revised form 7 June 2023; Accepted 9 August 2023
Available online 10 August 2023

systems [11] have been conducted. The results determined that the designs of the LHTES unit, the thermophysical characteristics of PCMs, and the temperature and velocity of the fluid had a considerable influence on the thermal performance of the LHTES unit. Organic [12], inorganic [13], and eutectic PCMs are the three most common forms. The organic PCM is an ideal compromise; paraffin wax, which has a high latent heat, is non-toxic, inexpensive [14] compared to other PCMs, chemically stable, and abundantly available in nature.

PCMs are restricted by their poor thermal conductivity, which varies between 0.1 and 0.8 W/(m K) [15]. Despite their remarkable energy storage capacity and efficiency, their low thermal conductivity caused energy storage rates significantly slow. As a consequence, choosing the best heat transfer augmentation method is crucial. Matrix fins, Microcapsulation, carbon-fiber brushes, heat pipes, carbon nanotubes, and metal nanoparticles are some of the possible solutions [16]. In an interesting idea, Li et al. [17] focused on enhancing the melting process of a horizontal latent heat energy storage system, using a triplex-tube unit with a flip mechanism. Numerical simulations validated by experimental data show that a single flip at a dimensionless time of 0.4576 can notably improve melting performance, reducing total melting time by 16.17% and increasing average heat absorption rate by 14.7%. However, this results in a slight 3.85% decrease in total heat absorption. Despite the trade-off, the flip mechanism makes the melting process more uniform and mitigates the impact of hard-to-melt zones. PCM-impregnated metal foams have been studied intensively [18]; for improving the overall heat conductivity of the system, metal foams appear to be a practical choice [19].

Buonomo et al. [20] numerically studied LHTES performance, including and excluding aluminum foam. According to the results, aluminum foam improves overall heat transfer by two compared to a pure enclosure. Pourakabar and Darzi [21] examined PCM phase change in an elliptical LHTES configuration. PCM with 90 and 70% porosities had 89 and 91.5 percent melting durations shorter than pure PCM. Sardari et al. [22] computationally evaluated the influence of copper foam porosity and foam arrangement on PCM's melting. Yang et al. [23] experimentally examined the PCM melting properties incorporated in foam made of copper. The findings indicate the rectangular container's angle of inclination did not influence melting characteristics.

Moussa and Karkri [24] numerically explored the phase transition kinetics of metal foam PCM (MFPCM) inside a rectangular container. Compared to PCM composites with constant heat flow, MFPCM with sinusoidal heat flow demonstrated a shorter melting time. They [25] also observed that the overall heat transfer reduced when the pore density of composite PCM rose. Using a vertical shell-tube LHTES design, Wang et al. [26] examined the impacts of porosity foam made of copper on PCM melting rates. Compared to uniform porosity, gradient porosity reduced melting time by 37.6%. Singh et al. [27] also statistically tested the influence of a nano PCM and fins in a conical shell. Several studies have analyzed the influence of tube design on LHTES thermal behavior. Mahdi et al. [28] analyzed an LHTES unit that consists of modules containing PCMs considering fusion temperatures. Various PCMs with a wide range of melting points improved the LHS. Multi-PCMs combined with nanoadditives and a cascaded foam metal resulted in the finest progress.

To discover the influence of geometrical designs on PCM phase change, Nie et al. [29] constructed seven vertical shell-tube LHS devices. This paper examines the performance of the composite and pure PCM. Conical shells improve natural convection over cylinders, while frustum tube systems improve heat conduction and convection over cylinders. Geometry adjustment showed a minimal influence on the thermal performance of MFPCM. The total melting time decreases with geometry change by less than 5.9% for MFPCM and within 9.2% for pure PCM compared to the cylinder LHS system. Bianco et al. [30] evaluated finned and non-finned metal foam to optimize heat transfer rate; they discovered that the finned metal foam at equal pumping power could dissipate heat at a rate around 3.3– 3.5 times the rate of the metal foam. A study by Huang et al. [31] revealed that the fin MFPCM provided superior heat transfer compared to the fin PCM. Metal foam with 90% porosity improved MFPCM performance.

Qureshi et al. [32] examined the heat transfer capabilities of three triply periodic cover-based foams utilized in an exemplary MFPCM system with those of the standard MFPCM. These findings indicate that the new designs significantly enhance LHTES performance by improving the average heat transfer coefficient and shortening the melting time of the PCM. Li et al. [33] presented a novel design of MFPCM for improved LHTES systems with Nano-Encapsulated Components (NEPCM). They considered the porosity of foam in evaluating the heat transfer capabilities of meta foam-NEPCM. Abandani and Ganji [34] investigated the melting behavior of three-layered PCMs with different melting temperatures within a heat exchanger.

Several thin-film MFPCM systems have recently been developed for cooling CPUs, GPUs, tablets, laptops, and electronic components [17]. Dede and Joshi [18] used MFPCMs to create battery cells that produce increased electricity while operating at a lower temperature. This invention could increase energy production while extending the lifespan of batteries. Sutradhar et al. [35] simulated transient and continuous heat load conditions for a rectangular MFPCM TES using an analytical model. Yan et al. [36] investigated how the metal foam structure influences the experimental temperature-controlling ability of the MFPCM. Zhuang et al. [37] assessed the heat transmission capabilities of a hybrid LHS, which included PCM, metal foam, and nanoparticles, in a cubic cavity with an internal heater. Naldi et al. [38] analyzed the discrepancies between experimental data and numerical conclusions by employing the most commonly used correlations for four distinct composite PCMs. Ashakibi et al. [39] studied the impacts of PCMs blended with copper and aluminum foam on the temperature reduction of solar panels. In addition, the impacts of foam porosity, PCM thickness, and metal foam type are investigated.

Some researchers [36–39], among others, have undertaken research on the use of MFPCMs for thermal energy storage. Yan et al. [36] examined how the structure of metal foam affects the temperature-controlling capability of metal foam-based phase transition materials. Zhuang et al. [37] evaluated the heat transfer capacities of a hybrid LHS consisting of PCM, metal foam, and nanoparticles. Using regularly used correlations for four separate composite PCMs, Naldi et al. [38] evaluated the differences between experimental data and numerical findings. Ashakibi et al. [39] investigated the effects of PCMs mixed with copper and aluminum foam on solar panel temperature decrease, as well as the effects of foam porosity, PCM thickness, and metal foam type.

Baruah et al. [40] developed a new design for encapsulated PCM containing metal foam structures implanted in PCM. In a rectangular system with varying degrees of inclination, Huang et al. [41] explored the heat transfer properties and melting of an MFPCM composite. Hafiz Muhammad [42] investigated different sink configurations that used nickel foam and paraffin wax to enhance the heat management of electronic components.

Du et al. [43] explores ways to improve the thermal conductivity of phase change materials, critical for large-scale latent heat storage technology. Using a 3-D numerical model, they compare four structures - pure paraffin, fin, metal foam, and fin-metal foam within a square latent heat storage device. The results reveal significant reductions in melting time (47.48%, 79.53%, and 83.68%) and increased temperature uniformity (28.97%, 79.37%, and 91.12%) with fin and metal foam additions. However, total heat storage decreases slightly (6.0%, 4.6%, and 11.64%). Additional dynamic temperature studies confirm the benefits of fins and metal foam in enhancing melting performance, despite the trade-off in heat storage.

Nonetheless, the literature review above indicates that metal foam improves the heat transfer efficiency of PCMs. However, metal foams reduce an energy storage unit's latent heat capacity since they cannot store latent heat and tend to suppress the natural convection flows by increasing resistance to fluid flow. Furthermore, filling metal foam takes

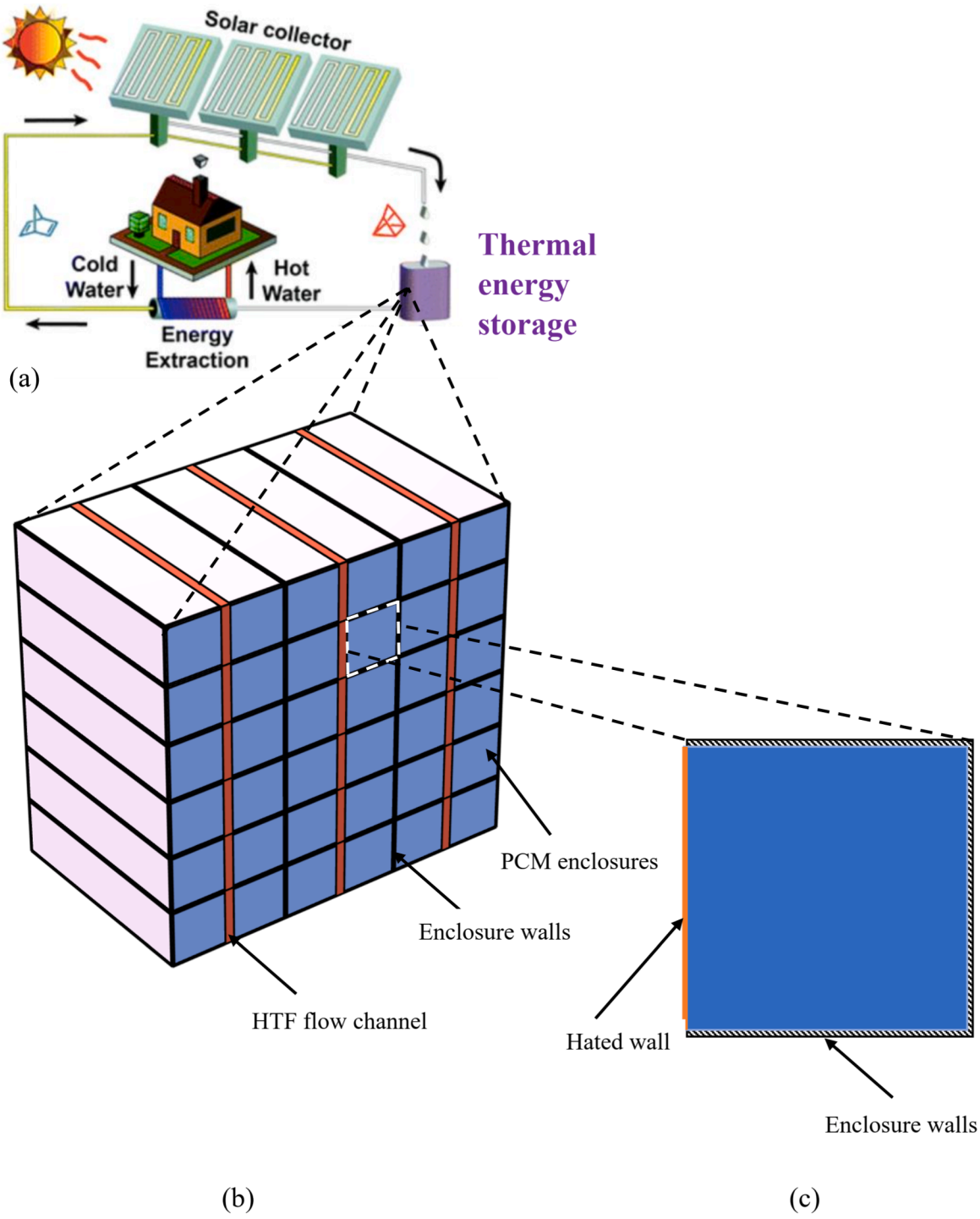

Fig. 1. The thermal energy storage for domestic hot water storage: (a) a simple solar hot water cycle, (b) the proposed LHTES design (3D); (c) a 2D schematic representation of the heat transfer model in the LHTES.

up a portion of the PCM volume, increasing the system's weight. However, there is a scarce number of research on using MFPCM layers with different porosities. This study aims to determine the impact of metal foam layers configuration in an enclosure to reduce the charging time while maintaining storage capacity. The highest thermal energy can be achieved by using less metal foam in one of the layers.

2. Model description and mathematical model

2.1. Description of the physical model

An LHTES has various industrial and domestic energy cycle applications. Here, Fig. 1(a) shows a simple loop of solar heat production where the solar heat received in the collectors and heats a working fluid. The working fluid enters an LHTES unit and moves toward the building.

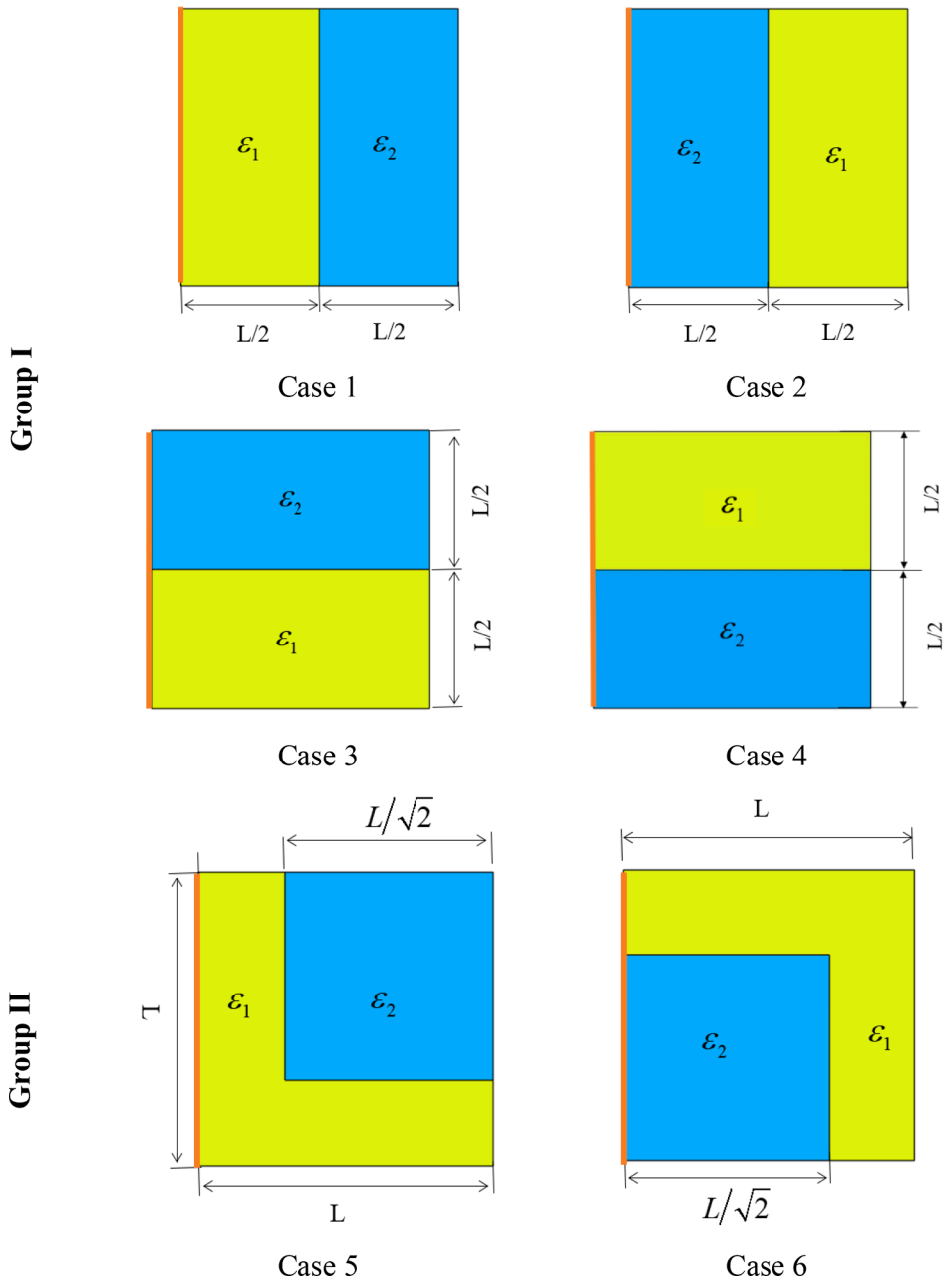

Fig. 2. The possible configurations of metal foam layers (ε_1 and ε_2) for three proposed groups splitting into half (I), an L shape division (II), and splitting diagonally (III).

The building extracts the heat from the working fluid through a heat exchanger. Then the warm working fluid enters the collectors to be reheated. The LHTES unit absorbs the excess heat of working fluid when the solar heat production is higher than the building demand. Later, when solar energy is unavailable or insufficient, the LHTES releases its stored heat. Fig. 1(b) depicts a 3D view of an LHTES design for fast charging/discharging purposes. The LHTES unit is rectangular channels filled with composite PCM-metal foam where the working fluid can flow between the channels. Fig. 1(c) depicts a 2D model of the LHTES. The 2D model is a square cavity of size $L = 120$ mm, where all walls are insulated except a vertical wall exposed to the hot working fluid and maintained at a hot temperature T_h.

The high metal foams' thermal conductivity enhances the overall thermal conductivity of the MFPCM and accelerates the charging process (melting of paraffin wax). Each PCM channel can be filled with two different copper foams with porosities ε_1 and ε_2. Then the PCM, paraffin wax, is filled inside the metal foams. Here, the aim is to find the best configuration of metal foam layers to yield the shortest charging time and the highest rate of thermal energy storage. Fig. 2 shows 12 proposed configurations for the metal foam layer layouts. These proposed designs are grouped into three categories splitting into half (group I), an L shape division (group II), and splitting diagonally (group III). The metal foam configuration impacts the melting rate in two major ways. The metal foam with different porosities results in different composite thermal conductivity (effective PCM thermal conductivity). A low-porosity metal foam is more thermally conductive than a high-porous metal foam. Thus, different layers pass the heat differently. Besides, a high porosity open-cell metal foam layer is less dense, allowing better natural convection circulation and contributing to convection heat transfer. The present study aims to find a configuration of metal foam layers

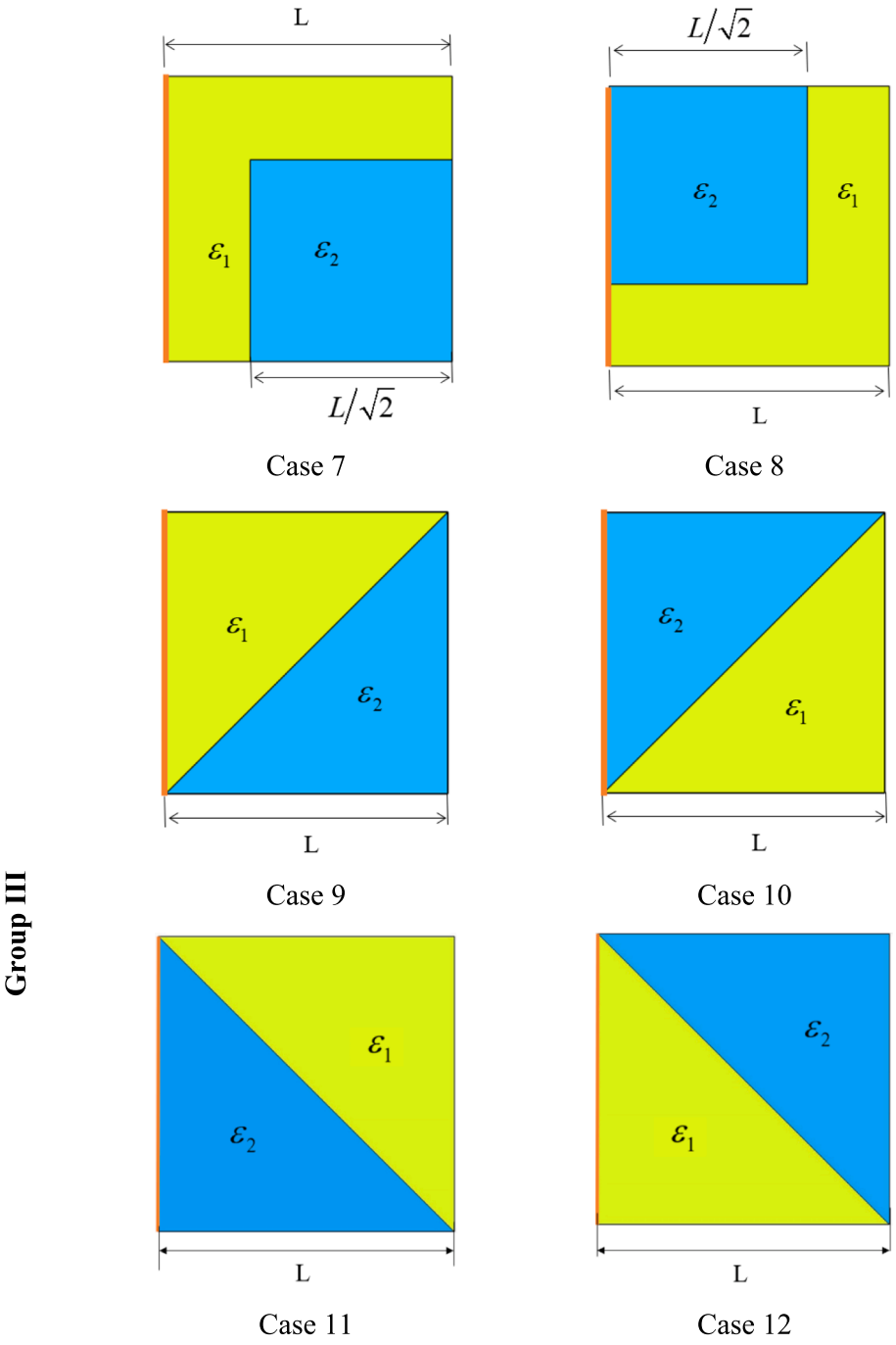

Fig. 2. (*continued*).

Table 1
Thermophysical properties of copper and paraffin wax [50].

Properties	Copper foam	Paraffin Wax
ρ_{PCM} (kg.m^{-3})	8900	900
μ_l (Pa.s)	–	0.0324
C_p (J.kg^{-1}.K^{-1})	386	2300
k (Wm^{-1} K^{-1})	380	0.3
ρ_{PCM} (kgm^{-3})	8900	900
h_f (kJkg^{-1})	–	148.8

benefiting from the highly effective thermal conductivity of low porous metal foams and the high permeability and convection heat transfer capability of high porous metal foams (with lower effective thermal conductivity). The horizontal and vertical division configurations were selected to allow two different heat conduction channels perpendicular and parallel to the heated wall. This allows an uneven melting in the enclosure with the hope of commencing a natural convection flow in the high porosity layer. The triangular layer configuration was selected to accelerate the melting using low porosity later at the top and to build a potential natural convection circulation for the second high porosity layer. The L shape configuration can make more complex melted areas during the charging process and may be useful for boosting the natural convection for the high porous layer.

The simulation of phase change thermal energy storage is computationally expensive. It takes weeks to simulate a single case. In the present study, the impact of a metal foam layer on the storage and heat transfer rate is investigated. Since the heat storage capacity and heat

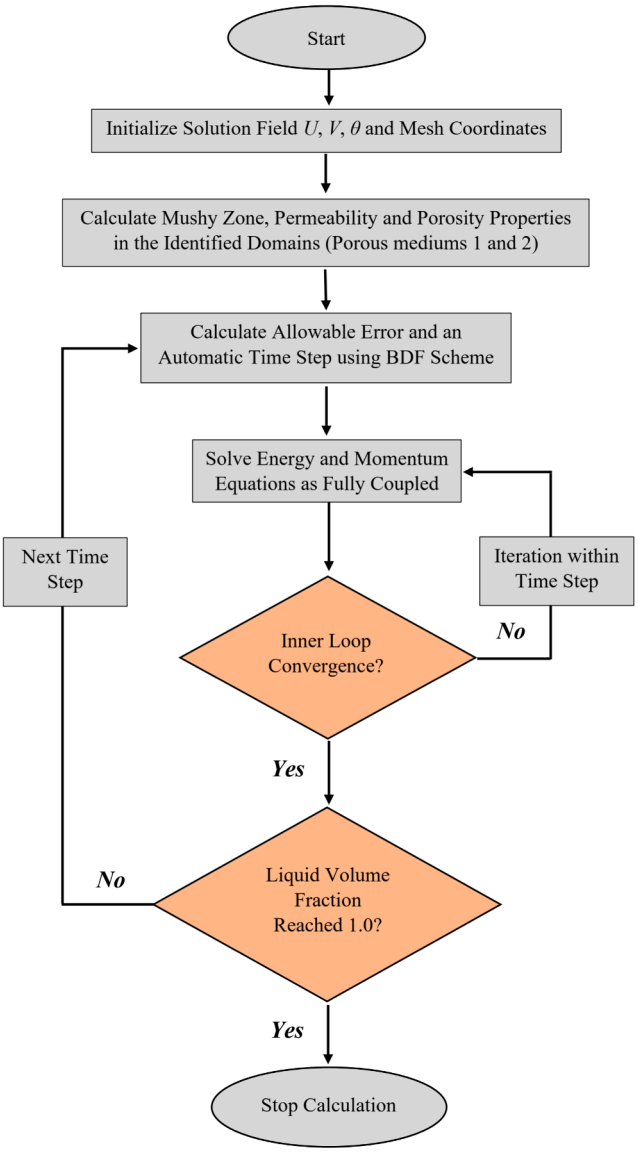

Fig. 3. The diagram of the solution method.

Table 2
The details of the selected meshes for mesh sensitivity analysis.

$M \times N$	Cell numbers	Edge elements	MVF @800 s	TES (kJ) @800 s
80 × 80	6400	400	0.937	4066
120 × 120	14,400	600	0.944	4100
160 × 160	25,600	800	0.947	4112
200 × 200	40,000	1000	0.948	4116

transfer rate of each unit are estimated using simulations, the estimated data can be directly employed for designing a larger system composed of multiple units. For instance, the heat capacity of a larger system, whether for domestic or industrial applications, is the accumulated total of the capacities of the individual units used. Similarly, the heat transfer rate of the larger system is the sum of the heat transfer rates from the individual domains.

2.2. Governing equations

The governing equations consist of flow and heat transfer in a porous medium. The flow in the porous medium is modeled using the Darcy-Brinkman model, which is similar to the Navier-Stokes equations, but it also has a source term (f_{Darcy}) which explains the Darcy flow resistance. In a solid region, the velocity of fluid movement is heavily impeded by the sink term, which creates a significant resistance force and brings the velocity to zero. This study employs the thermal equilibrium model of MFPCM, which disregards the temperature differential between the metal foam and PCM inside the pores. Even though local thermal non-equilibrium (LTNE) models may represent temperature differences between two materials during melting, empirical research suggests that the LTNE condition is only important at the beginning of the melting process [44]. Furthermore, experimental and computational investigations [45–47] demonstrate that the LTNE condition becomes less significant as the melting process advances. The local thermal equilibrium (LTE) model is often utilized for thermal energy storage applications for its simplicity and fair modeling accuracy. Considering the above model, the governing equations for the conservation of mass, momentum, and energy are given by [48–50]:

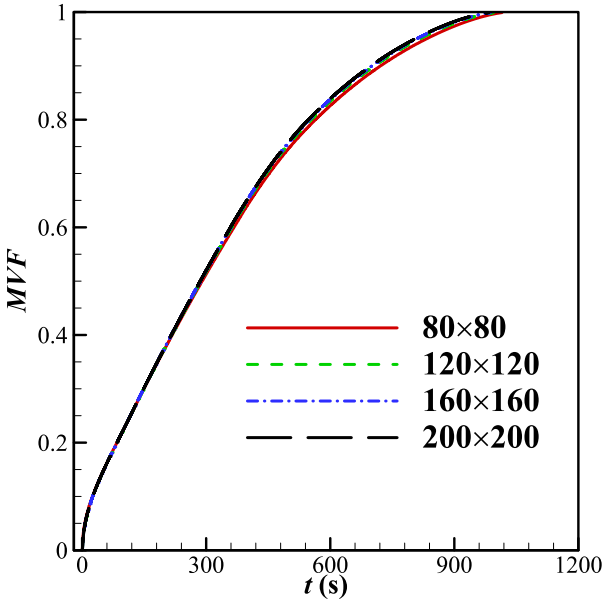

Fig. 4. The MVF over time for various mesh sizes.

Conservation of mass:

$$\left(\frac{\partial u_{\mathrm{i}}}{\partial x_{\mathrm{i}}}\right) = 0 \tag{1}$$

Conservation of momentum:

$$\frac{\rho_{\mathrm{PCM}}}{\varepsilon}\frac{\partial u_{\mathrm{i}}}{\partial t} + \frac{\rho_{\mathrm{PCM}}}{\varepsilon^2}\left(u_{\mathrm{j}}\frac{\partial u_{\mathrm{i}}}{\partial x_{\mathrm{j}}}\right) = -\frac{\partial P}{\partial x_{\mathrm{i}}} + \left[\frac{\partial}{\partial x_{\mathrm{j}}}\left(\frac{\mu_{\mathrm{PCM}}}{\varepsilon}\frac{\partial u_{\mathrm{i}}}{\partial x_{\mathrm{j}}}\right)\right] + f_{\mathrm{Darcy,i}} + f_{\mathrm{sink,i}} + f_{\mathrm{b,i}} \tag{2}$$

Conservation of energy:

$$(\rho c_p)_{\mathrm{eff}}\frac{\partial T}{\partial t} + (\rho c_p)_{\mathrm{PCM}}\left(u_{\mathrm{i}}\frac{\partial T}{\partial x_{\mathrm{i}}}\right) = \frac{\partial}{\partial x_{\mathrm{i}}}\left(k_{\mathrm{eff}}\frac{\partial T}{\partial x_{\mathrm{i}}}\right) + h_{\mathrm{source}} \tag{3}$$

where u_{i} is the velocity components in an i direction where i = 1 and 2 denote the x and y directions, respectively. The dynamic viscosity (μ), density (ρ), specific heat capacity (c_{p}), and thermal conductivity (k) are the thermophysical properties. The subscripts PCM and eff indicate the PCM and effective thermophysical properties of the composite-PCM, respectively. The subscripts Dacy, sink, b, and source denote the Darcy force, the sink term, the buoyancy force, and the heat storage due to the phase change. Here, f_{Darcy} accounts for the Darcy force resistance against the fluid motion in the metal foam in x or y directions (i direction). f_{sink} exerts a huge force against the fluid motion in the solid regions, which

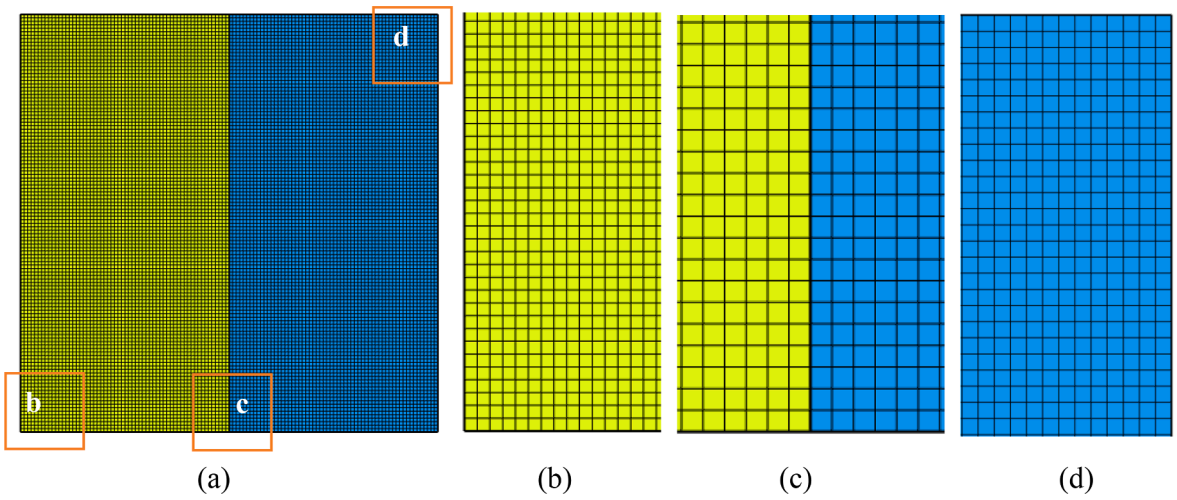

Fig. 5. Views of mesh with size 120 × 120 for case 1; (a) A full view of mesh. Important mesh regions are marked in (a) and then a zoomed view of these regions is depicted as. (b) the bottom corner of mesh; (c) the mesh at the interface of two metal foam regions; (d) the top right corner.

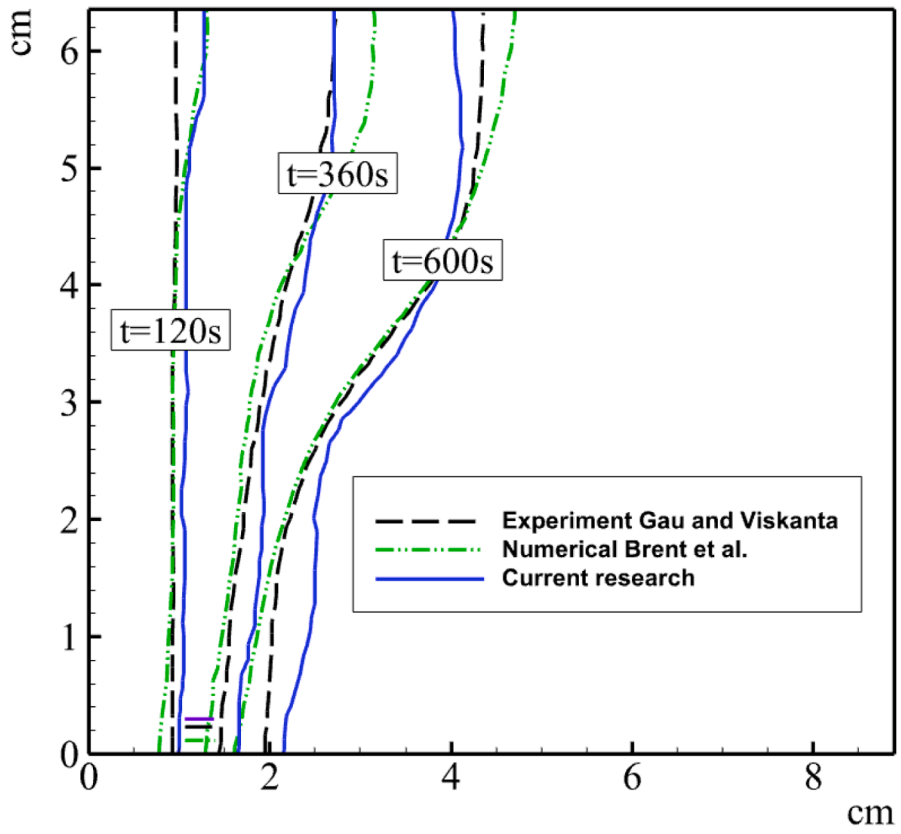

Fig. 6. A comparison of this investigation's results with those of Gau and Viskanta's experimental study [48] and Brent et al.'s numerical study [49].

leads to negligible (zero) fluid velocity in the solid regions. f_{sink} disappears from equations in the liquid regions. Finally, f_{b} induces a body force on the fluid due to the temperature changes and causes the natural convection flows. The term h_{source} takes into account the latent heat energy due to the phase change. These terms in the governing equations are introduced as [48–50]:

$$f_{\text{Darcy,i}} = -\frac{\mu_{\text{PCM}}}{\kappa}u_{\text{i}}\,,\quad f_{\text{sink,i}} = -A_{mush}\frac{1-2\theta(T)+\theta^2(T)}{\lambda+\theta^3(T)}\,.\,u_{\text{i}}, \tag{4a}$$

$$f_{\text{b,i}} = \begin{cases} 0 & \text{i} = 1 \\ \rho_{\text{PCM}} g \beta_{\text{PCM}} (T - T_f) & \text{i} = 2 \end{cases} \tag{4b}$$

and.

$$h_{\text{source}} = \varepsilon \rho_{\text{PCM}} \text{L}_{\text{f}} \frac{\partial \theta(\text{T})}{\partial \text{t}} \tag{4c}$$

The latent heat of fusion (L_f), volumetric thermal expansion (β), and fusion temperature (T_f) are thermophysical properties. Moreover, $g = 9.81\ \text{m/s}^2$, $A_{mush} = 10^{10}\ (\text{Pa·s/m}^2)$ and $\lambda = 0.001$. The volume fraction of

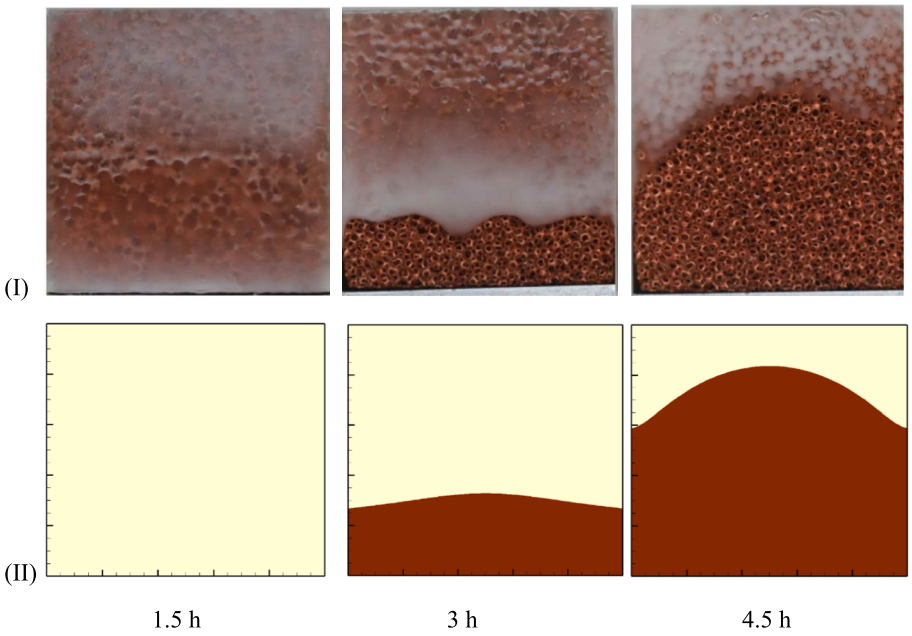

Fig. 7. The paraffin wax phase change embedded in copper foam from the bottom 1.5, 3, and 4.5 h after heating. A comparison between experiments of Zheng et al. [50] (with permission from Elsevier) and (II) the current simulations.

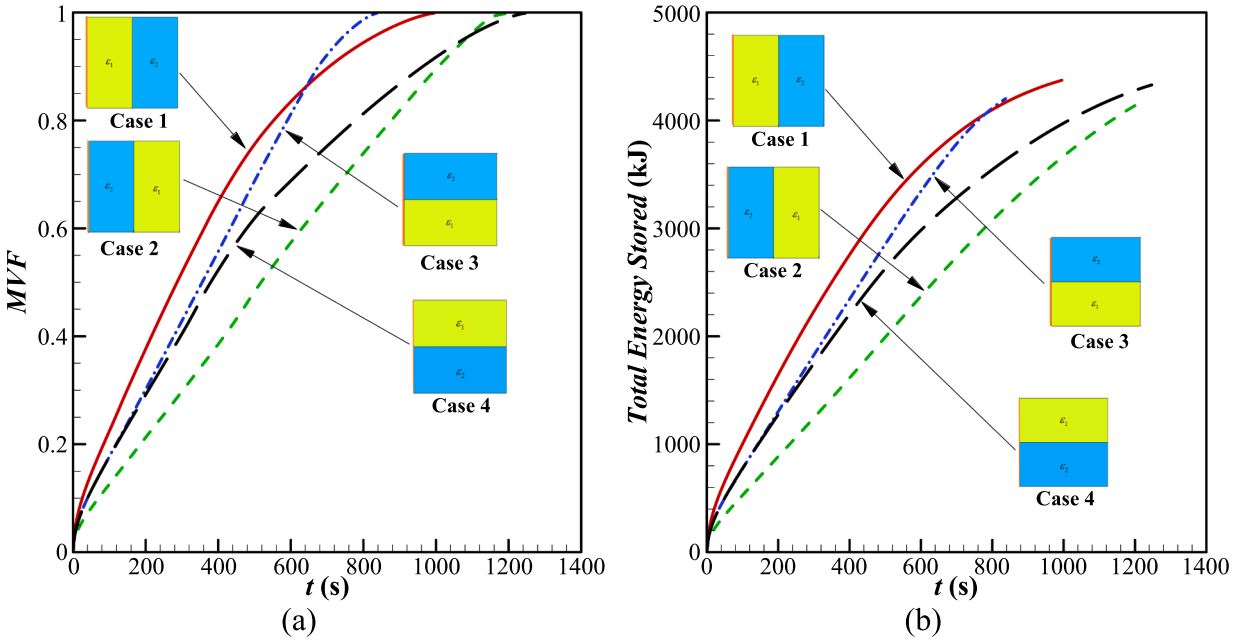

Fig. 8. The characteristics curves for group I: (a) Melting volume fraction, (b) Total stored energy.

molten PCM, θ, is introduced as:

$$\theta(T)=\begin{cases}0 & T<(T_f-\Delta T_f/2)\\ \left(\dfrac{T-T_f}{\Delta T_f}\right)+\dfrac{1}{2} & (T_f-\Delta T_f/2)\langle T<(T_f+\Delta T_f/2)\\ 1 & T>(T_f+\Delta T_f/2)\end{cases} \tag{5}$$

where $\theta=1$ indicates a fully melted PCM, and $\theta=0$ indicates a fully solid PCM. ΔT_f denotes the phase change temperature range. The porosity (ε) and permeability (K) depend on the metal foam layer and are computed as:

$$\varepsilon=\begin{cases}\varepsilon_1 & \text{layer 1}\\ \varepsilon_2 & \text{layer 2}\end{cases},\ \text{and}\ K=\begin{cases}K_1 & \text{layer 1}\\ K_2 & \text{layer 2}\end{cases} \tag{6}$$

The thermophysical properties of paraffin wax in the solid and liquid regions were considered constant, according to Table 1. The effective heat capacity and thermal conductivity of the MFPCM are computed as:

$$(\rho C_p)_{\text{eff,PCM}}=(1-\varepsilon)(\rho C_p)_m+\varepsilon(\rho C_p)_{\text{PCM}} \tag{7}$$

The effective thermal conductivity was evaluated from [51]:

$$k_{\text{eff}}=\frac{1-\gamma}{\left(\frac{1-\varepsilon}{k_m}+\frac{\varepsilon}{k_{PCM}}\right)}+\gamma((1-\varepsilon)k_m+\varepsilon k_{PCM}) \tag{8}$$

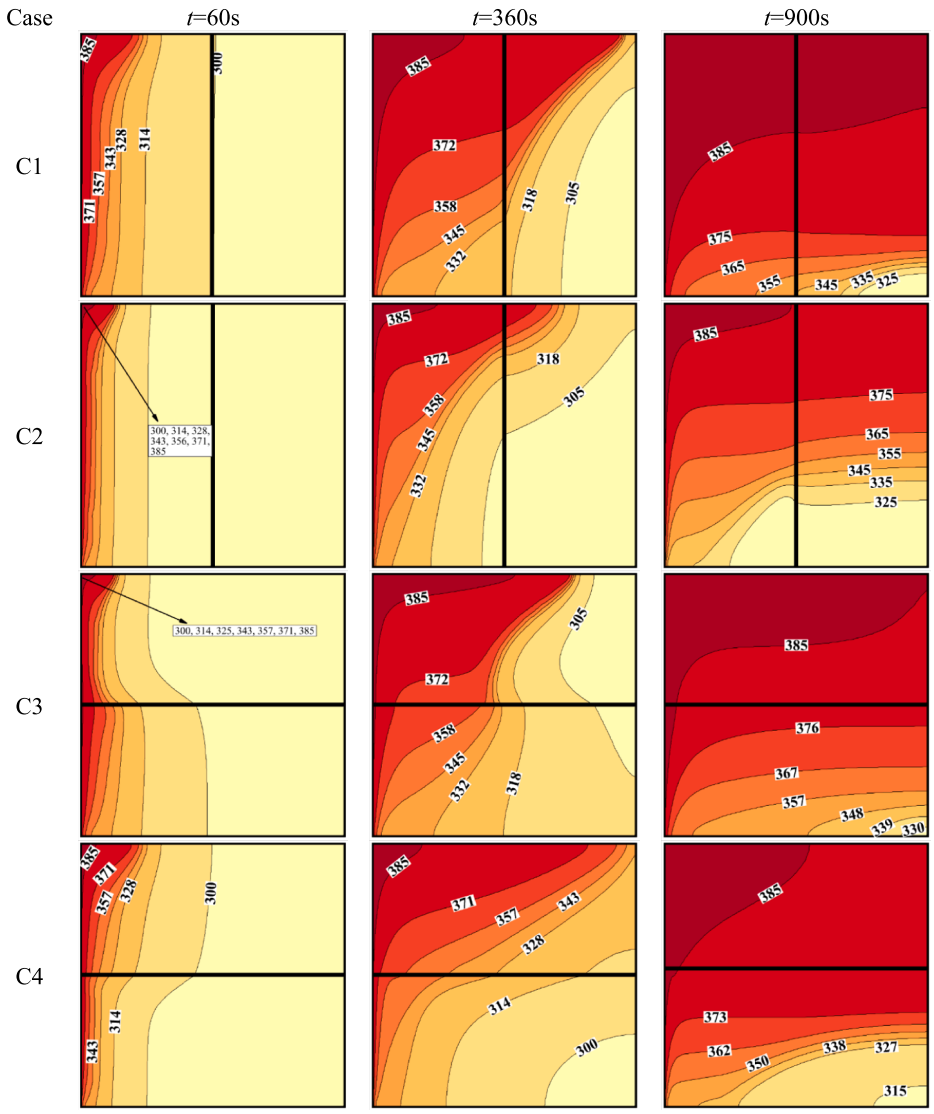

Fig. 9. Temperature contours for group I.

where $\gamma = 0.35$ [51]. Eq. (8) is in good agreement with the practical observations of [52]. The subscript m denotes the metal foam. Besides, the porous permeability was obtained by invoking [53]:

$$K = d_p^2 \frac{73 \times 10^{-5}}{(1-\varepsilon)^{0.224}} \left(d_l d_p^{-1}\right)^{-1.11} \tag{9a}$$

$$\left(d_l d_p^{-1}\right) = 1.18 \left(\frac{1-\varepsilon}{3\pi}\right)^{0.5} [1 - \exp(-(1-\varepsilon)/0.04)]^{-1} \tag{9b}$$

where $d_p = 254 \times 10^{-4} \omega_p^{-1}$, and ω_p denotes the pore per inch characteristics of the porous (PPI), which was selected as 5 PPI. The permeabilities are also computed as $K_1 = 2.976\text{E-}7\ m^2$ and $K_2 = 4.117\text{E-}7\ m^2$. Moreover, $\varepsilon_1 = 0.9$ and $\varepsilon_2 = 0.975$.

The hydraulic imposed boundary conditions are the surface zero velocity. The thermal boundary conditions are zero heat flux at all surfaces except the heated surface where $T = T_h$. The initial condition is a uniform constant temperature $T = T_0$. In the current research, $T_h = 70\ ^\circ C$, $T_0 = 25\ ^\circ C$, and PCM fusion temperature is 54 °C. Besides, the copper metal foam and paraffin wax properties are listed in Table 1.

3. Verification of the code and numerical method

3.1. Numerical method

The partial differential equations are explained in Eqs. (1)-(3), along with the corresponding initial and boundary conditions, were integrated over a discretized mesh using the finite element method [54]. The Gauss quadrature elements were used to integrate the field variable and obtain the residual equations. The residual equations were solved for field variables in a coupled approach by employing the Newton method. Then, the timesteps and accuracy of the computations were controlled by the backward differential formula [55] consisting of a free order between 1 and 2 to keep the relative error lower than 10^{-4}. The details of the solution approach are explained in Fig. 3. The stop condition for computations was the total melting, which could be satisfied by MVF > 0.999.

3.2. Mesh sensitivity

A structured mesh with M mesh vertexes in the x-direction and N mesh vertexes in the y-direction was selected. Case 1 was chosen for mesh sensitivity analysis, and the impact of various mesh sizes on the results was explored. Table 2 shows the details of each examined mesh,

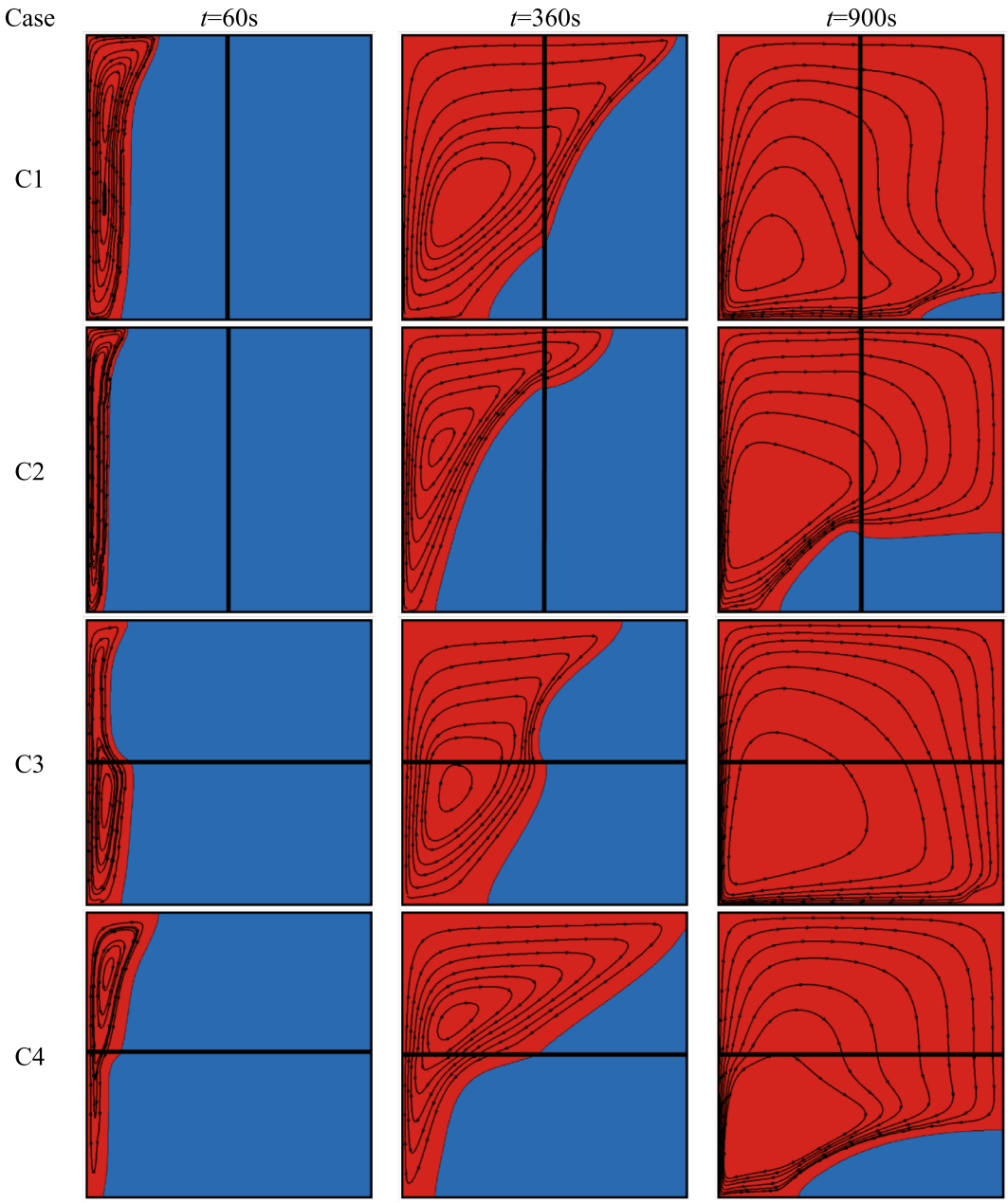

Fig. 10. Streamlines for group I.

the number of created cells, and the MVF and stored energy (TES) reported after 800 s of the melting process. Table 2 and Fig. 4 show that a mesh size of (120 × 120) could provide a fair accuracy and computational cost. Thus, the present research results are computed with a mesh size of 120 × 120. A general and detailed view of the adopted mesh is depicted in Fig. 5.

3.3. Validation and verification

The accuracy of the model and code used in this study was confirmed by comparing the results to previous research. Specifically, Gau and Viskanta conducted a study on the melting heat transfer of PCMs in a rectangular enclosure with a height of 63.5 mm and a width of 88.9 mm. In their experiment, the PCM was initially at a low temperature of 28.3 °C, and the left wall of the enclosure was exposed to a constant temperature of 38 °C.

An essential part of the research on phase-change processes is the investigation and measurement of the geometry of the solid–liquid interface. To do this, researchers have used two basic methods: the pour-out technique and probing. Pour-out involves stopping the phase-change process at predefined intervals and rapidly dumping out the liquid (melt). Certain external factors may affect the geometry of the solid–liquid contact when the liquid drains away. To get insight into the underlying physics of the phase-change process, researchers closely observe the geometry of the interface throughout this process. Fig. 6 shows the melting interface during the time reported by Gau and Viskanta [56], the numerical study of Brent et al. [57], and the current research results. As seen, the trend of the results agrees well. However, there are also some differences between the numerical and experimental results which may be attributed to the impact of the pour-out approach utilized for the interface measurements. In order to further evaluate the accuracy of the present model and simulations, the results were comparted with other literature works.

As another comparison, the results of current research for melting

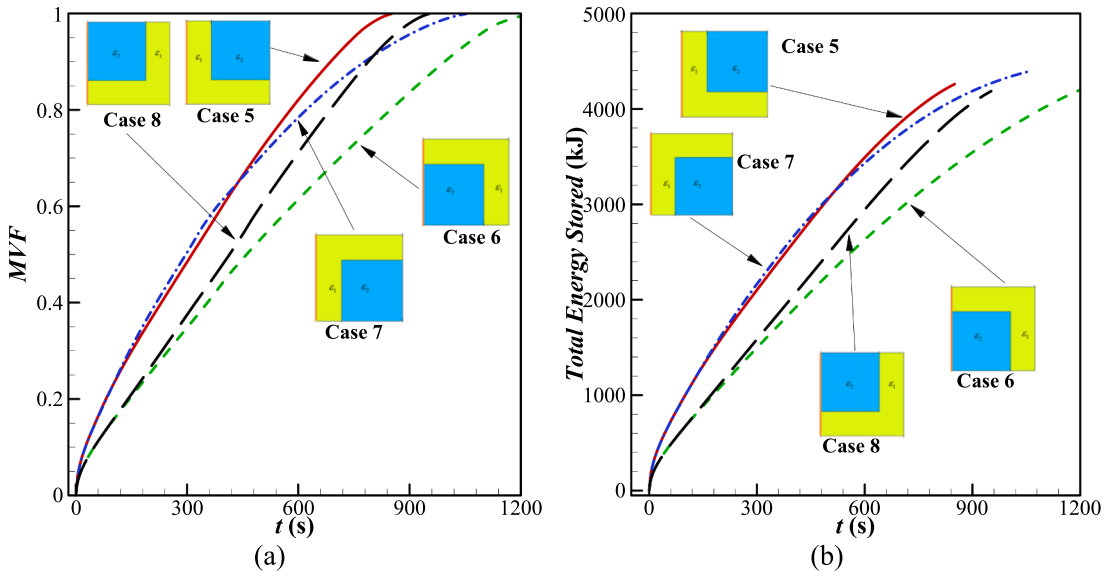

Fig. 11. The characteristics curves for group II: (a) Melting volume fraction and (b) Total stored energy.

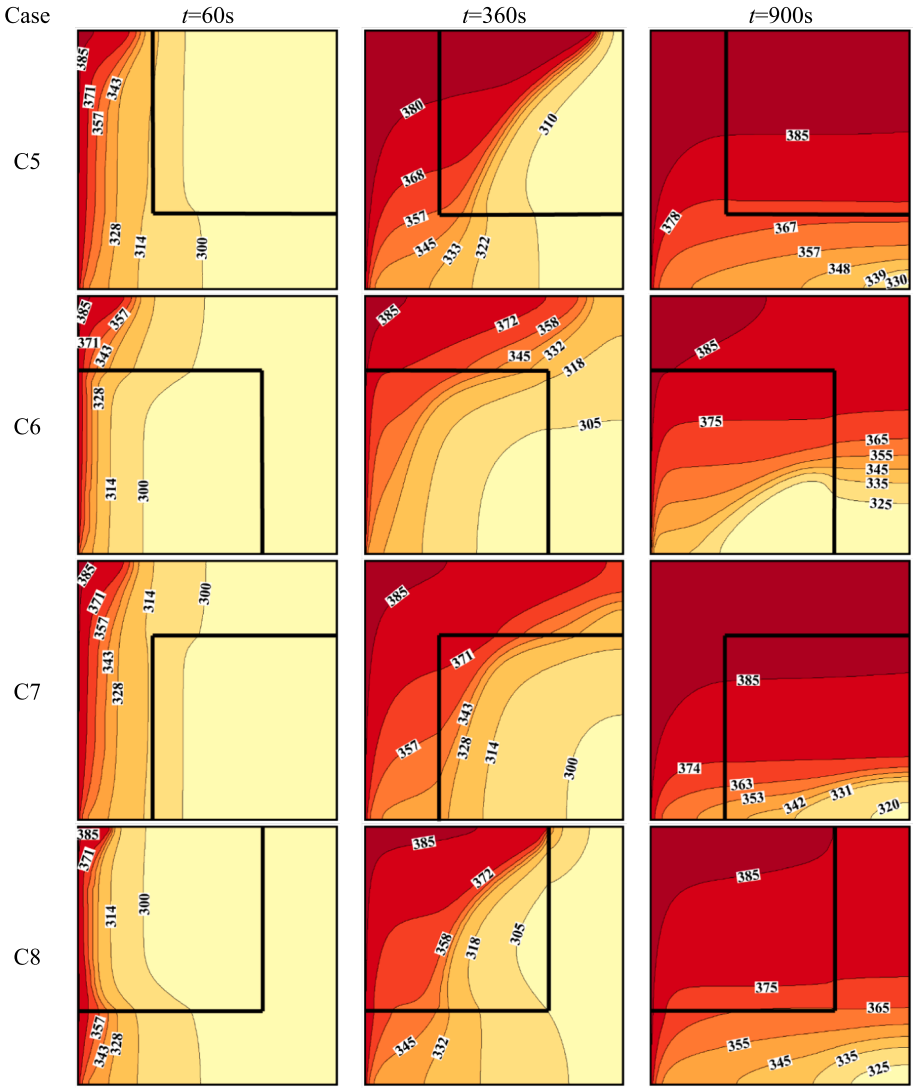

Fig. 12. Contour of isotherm for group II.

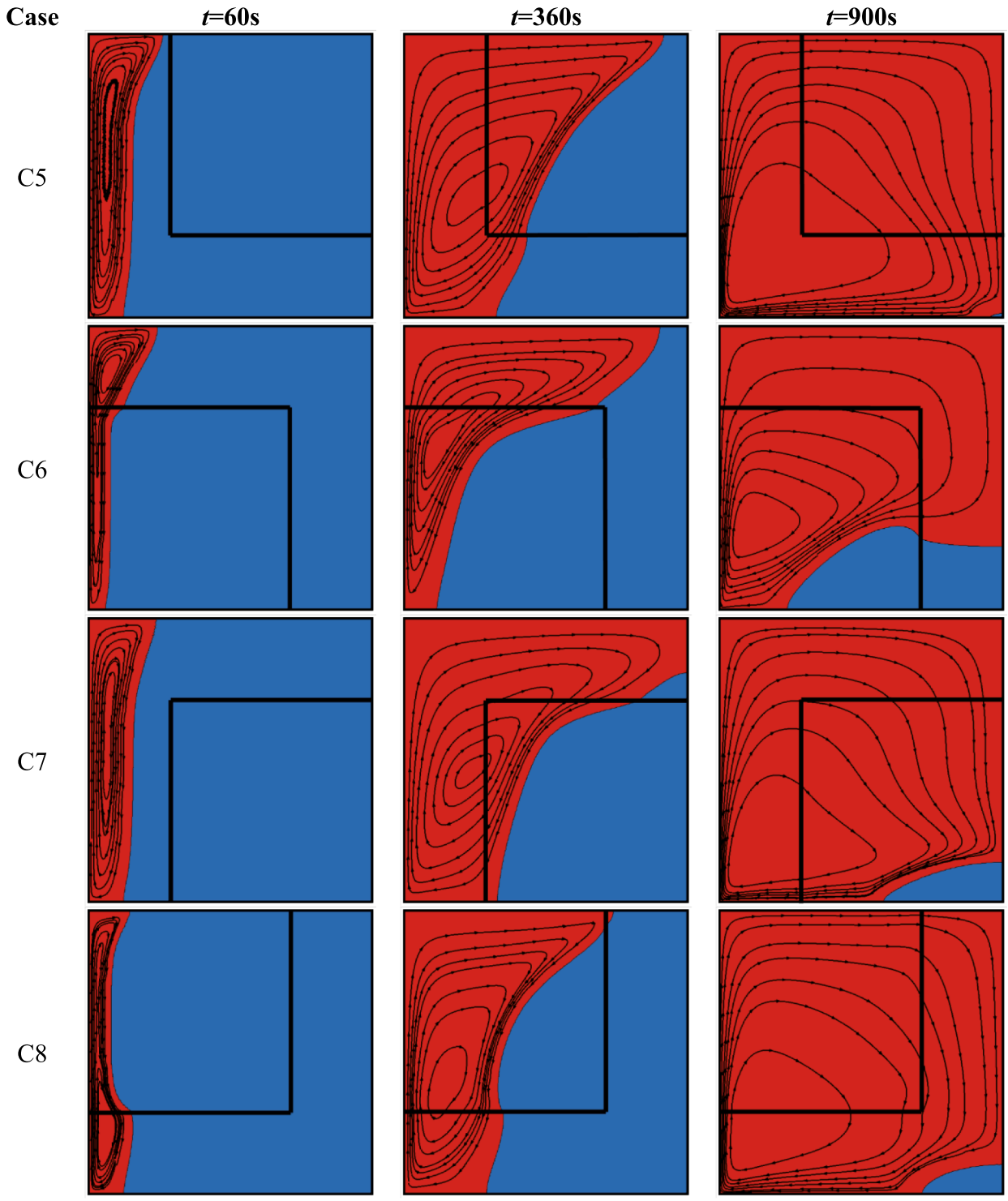

Fig. 13. Streamlines for group II.

paraffin in copper foam were compared with the experimental observations of Zheng et al. [50]. Fig. 7 depicts the melting of paraffin-copper foam from below in an enclosure of size 100 mm and a porosity of 97.5%. The melting interfaces computed in current research are in fair agreement with observations of [50]. However, there are some differences in the details of interface shapes between the experiment and simulations. These details could be due to small heat losses from the side walls of the enclosure and small heat flux fluctuation of the heater during the experiment.

4. Results and discussion

In this work, LHTES was studied with layers of metal foam arranged in several configurations distributed into 3 groups, each containing four different configurations. Thus, the total number of studied configurations is 12. Each configuration contains two types of metal foam with different porosity, the first porosity equal to 0.9 and the second porosity equal to 0.975. Metal foam (porous medium) is a cellular structure composed of interconnected ligaments to form a metal matrix. The lower the porosity of the metal foam, the greater the diameters of the

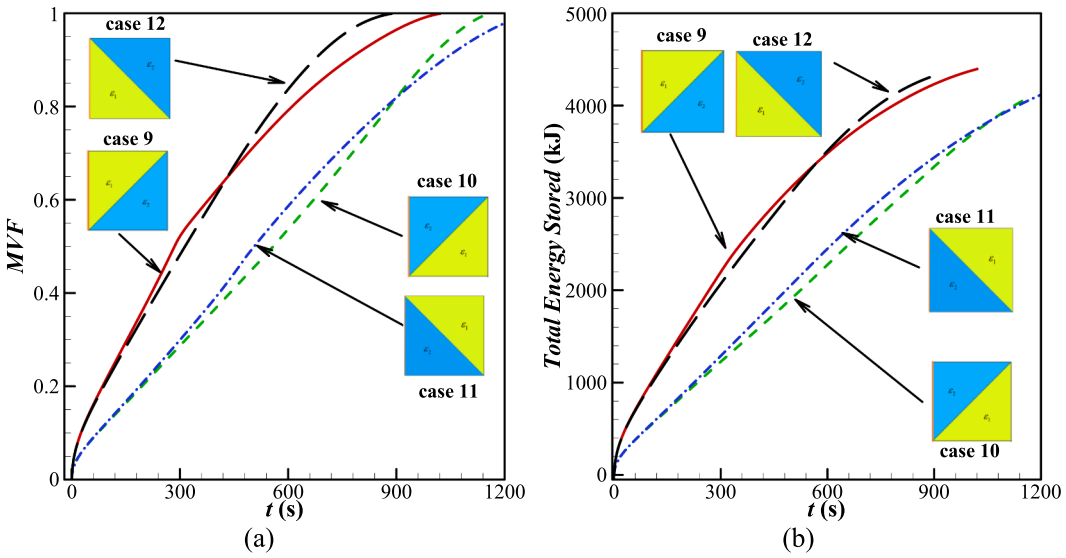

Fig. 14. The characteristics curves for group III: (a) Melting volume fraction, (b) Total stored energy.

ligaments. Thus, the surface area of heat transfer increases, the effective thermal conductivity increases, and the PCM volume decrease.

The first group (cases from 1 to 4) is discussed in figures from Fig. 8 to Fig. 10. In this group, the arrangement of metal foam layers is horizontal and vertical. Fig. 8 shows the melting volume fraction and the total energy stored. As can be seen, the melting process in cases 1 and 3 are completed faster than in cases 2 and 4. The fastest melting is in case 3, where the melting is completed by 837 s, while the slowest melting is in case 2, with a melting time of 1247 s. This means that the arrangements of this group can affect the completion of the melting time by about 7 min.

In case 1, the melting process of the PCM proceeds faster, but the steep slope has been reduced with increasing time, and more time is required to complete the melting. The melting process of case 3 continued with a slower slope than in case 1, where its slope remained constant until the end of the process and reached full melting earlier than in other cases. Here it is worth noting that the melting process of the PCM begins with the transfer of heat to it from the hot wall by conduction, and thus the layers of PCM adjacent to the hot wall melt first. The temperature of the PCM is greater at the top of the LHTES as a result of the effect of natural convection in the melted PCM, where the hot PCM with low density rises to the top. In contrast, the cold PCM with high density descends; thus, melting begins from the top of the LHTES and continues gradually to the bottom, and the lower right part that is distant from the hot wall is the last Melt part of the LHTES.

In case 1, the first porous medium (with the least porosity) is adjacent to the left vertical hot wall, while the second porous medium (with the higher porosity) is to the left. As depicted in Fig. 8, the melting fraction continued steeply. These results are the consequences of the improved heat transfer caused by the first porous medium with high effective thermal conductivity. Then, the molten PCM enters the second porous medium with a low effective thermal conductivity. Therefore, the slope gradually decreases, and reaching the bottom right of LHTES, requires a considerable time to melt completely. Instead, in case 3, the first porous medium covers the lower areas of LHTES. Since the melting is delayed at the bottom of LHTES, the first porous medium with a high effective thermal conductivity has solved this problem. According to the arrangement of a porous medium in cases 1 and 3, the progress of the melting front in the upper half of the LHTES (second porous medium) in case 3 continues more slowly than in case 1, due to the low porosity of this layer and lower effective thermal conductivity. This is while the melting front progresses in the lower half of the LHTES. Therefore, the melting time for case 1 to fully melt the bottom right of the chamber is much longer than in case 3. As a result, the MVF curve raises more smoothly for case 1, but case 3 continues with a constant slope until a full melt.

The full melting time for cases 2 and 4 is almost the same, but during the process, case 4 performed better than case 2. The first porous medium in the right half of the LHTES has caused the melting fraction curve of case 2 to approach case 4 in the final moments. On the other hand, the melt front in case 4 continued with a relatively steep slope until moments after leaving the first porous medium. However, melting the PCM located in the lower-right areas of the LHTES for Case 4 takes more time. As mentioned, cases 3 and 4 provide the shortest (837 s) and longest (1246 s) thermal charging times in group I. In comparison to the scenario where the light foam layer is placed at the bottom, positioning the light foam layer at the top (ε_2) decreases charging time by roughly 32%.

The total stored energy for cases from 1 to 4 of the first group is depicted in Fig. 8(b). It is clear that the obtained patterns completely follow the melting fraction patterns of cases from 1 to 4. The amount of stored energy is a function of the melting process of the PCM. The quicker the melting process, the shorter the energy storage time. Instead, if the melting front continues to slow down, more time is required to store energy. Hence, the stored energy pattern for cases 1 to 4 during the melting process follows the pattern for the melting fraction of the PCM. It is worth noting that changing the arrangement of the first and second porous medium did not impact the maximum stored energy and, in all four cases, stored more than 4000 kJ.

Fig. 9 shows the constant temperature lines for cases from 1 to 4 at time-snaps of the 60 s, 360 s, and 900 s. For cases 2 and 3, there are seven isotherm labels which the lowest temperature next to the wall and the highest temperature in the domain. The labels were not added over each line to avoid congestion. According to the results, the amplitude of the constant temperature lines at any time corresponding to the first porous medium is greater than the second porous medium. For example, the isotherms are wider in the left half of case 1 and the right half of case 2. A similar trend could also be in cases 3 and 4. The lower part of the LHTES in case 3 and the upper half of the chamber in case 4 had the largest width. Instead, the constant temperature lines for all four cases are compressed in the second porous medium. As mentioned, the second porous medium has less effective thermal conductivity than the first porous medium, so the possibility of developing constant temperature lines in the second porous medium is less than that in the first porous medium.

The flow lines and melting front for all four cases in the first group are shown in Fig. 10 at time snaps of the 60 s, 360 s, and 900 s. As can be

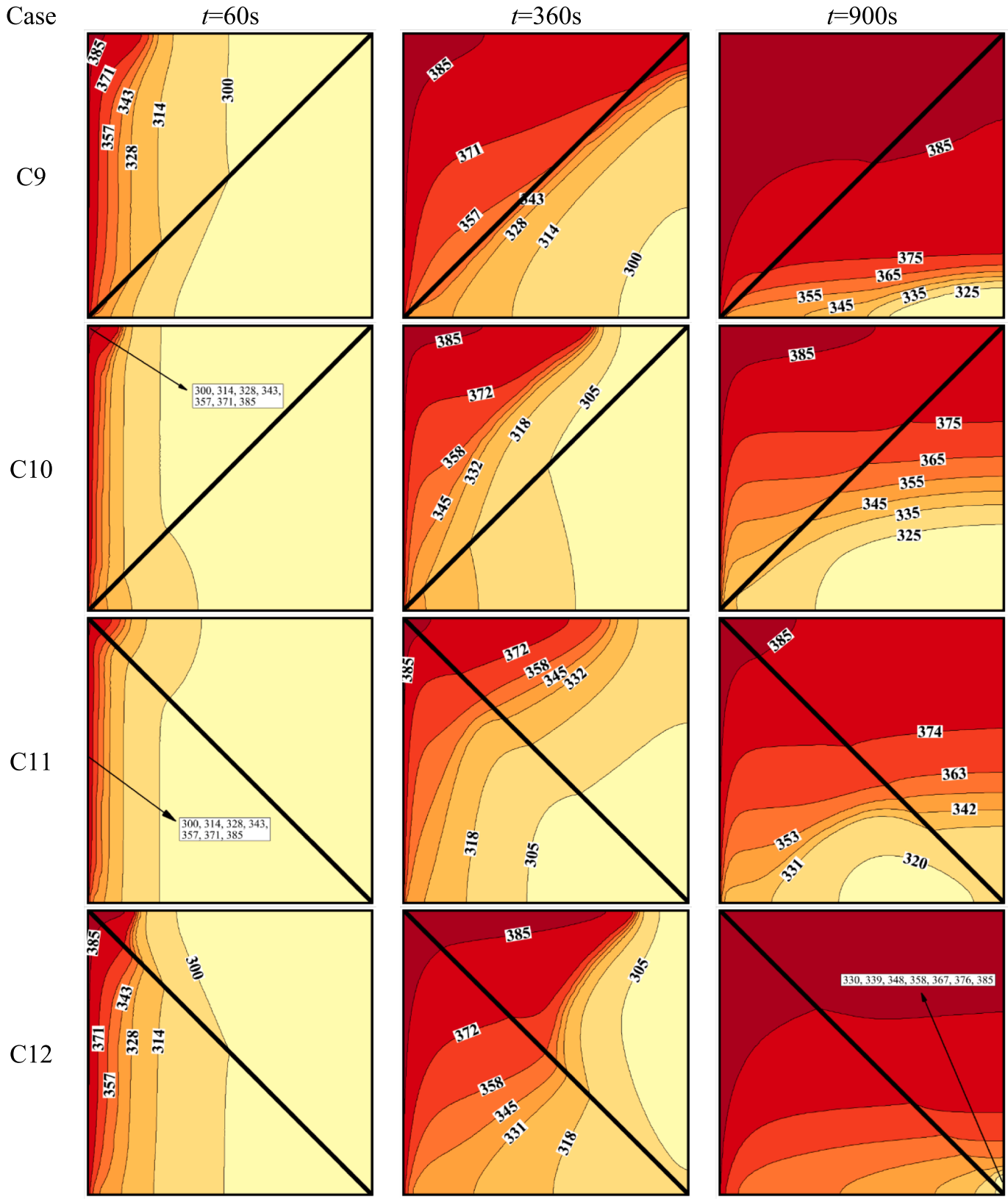

Fig. 15. Temperature contours for group III.

seen, in the beginning, the most natural pattern of the progress of the melting front and flow lines is related to cases 1 and 2.

Also, at the same time, depending on the placement of the first porous medium in the lower and upper parts of the LHTES for cases 3 and 4, respectively, the flow lines and the melting front in those halves are more advanced. At the time (360 s), regardless of the location of the first and second porous medium, the most progress of the melting front and the development of flow lines can be seen in the upper areas of the

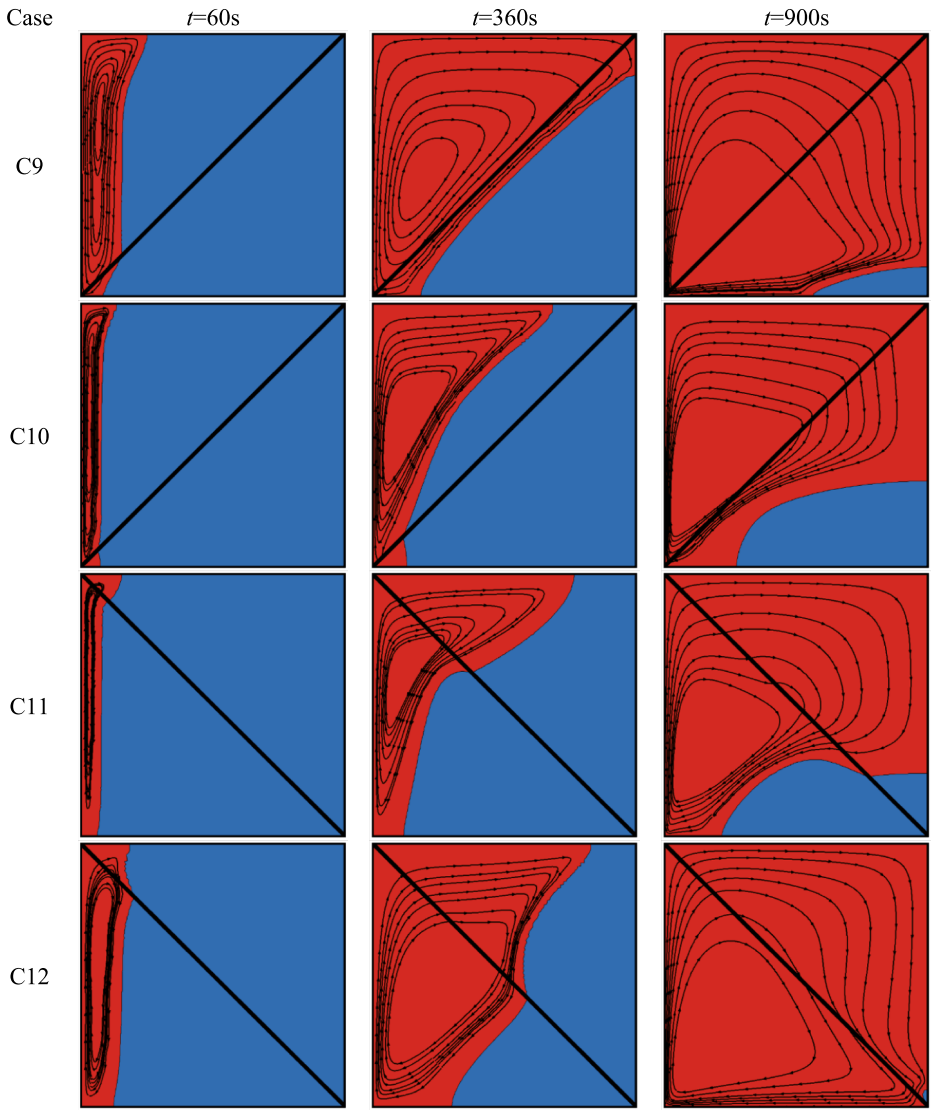

Fig. 16. Streamlines for group III.

LHTES. In the last time (900 s), only case 3 reached full melting. After that, case 1 is on the verge of completing the melting. Then comes cases 4 and 2, respectively. The results obtained in the category of Figs. 9 and 10 entirely agree with the results of Fig. 8.

To evaluate the second group, the melting fraction and the amount of stored energy in cases from 5 to 8 have been evaluated, as shown in Fig. 11. The fastest and slowest melts are in cases 5 and 6, which lasted (850 and 1226 s), respectively, while cases 7 and 8 are located between cases 5 and 6. As can be seen, the characteristic patterns of case 7 are very close to that of case 5, with up to 65% melting. After that, the slope decreases in case 7 and takes a longer time to complete the melting than in case 5 due to the existence of the second porous media in the lower right part. The first porous medium is adjacent to the hot wall in both cases. In case 5, the first porous layer covers the lower part of the LHTES, while in case 7, the first porous medium covers the upper part of the LHTES. As mentioned, a heavy porous media in the lower portions of the LHTES improves effective thermal conductivity. It causes the melting front to advance as much as possible.

As for cases 5 and 8, the first porous medium covers the lower part of the LHTES. However, the presence of the first porous medium in contact with only the lower part of the hot wall in case 8 makes the melting delayed compared to case 5. As mentioned above, the slowest melting case is case 6. In this case, which is diagonally symmetrical to case 5, the first porous medium is not adjacent to the bottom of the hot wall. Therefore, the thermal conductivity in the lower parts in case 6 is lower than in other cases.

On the other hand, the presence of the first porous media in the upper parts of this case makes the melting front advance quickly, but it does not impact the full melting time. Therefore, completing the melting process of the PCM, in this case, required more time than in other cases (cases 5, 7, and 8). The shortest (850 s) and longest (1226 s) melting times belong to cases 5 and 6, respectively. So, changing the foam layer configurations could reduce the thermal charging time by 30%.

As depicted in Fig. 11(b), the results trend of the stored energy follows the melting fraction of the PCM. Also, the last value recorded at the completion of the melting process for the four cases is approximately equal to 4000 kJ. The full melting for case 5 is achieved faster than in the other three cases. In this case, the amount of stored energy is achieved in a shorter time than in cases 6, 7, and 8.

Isotherms for the four cases from 5 to 8 of the second group are shown in Fig. 12 at three times-snaps of the 60 s, 360 s, and 900 s. As can be seen, the extension of the isotherms for case 5 in all three corresponding times is more than in the other three cases. The development of isotherms in case 7 is also better than in cases 6 and 8 in the first and second time-snaps, while in the last time, the melting front for case 8 is more significant than in case 7, in accordance with the results obtained

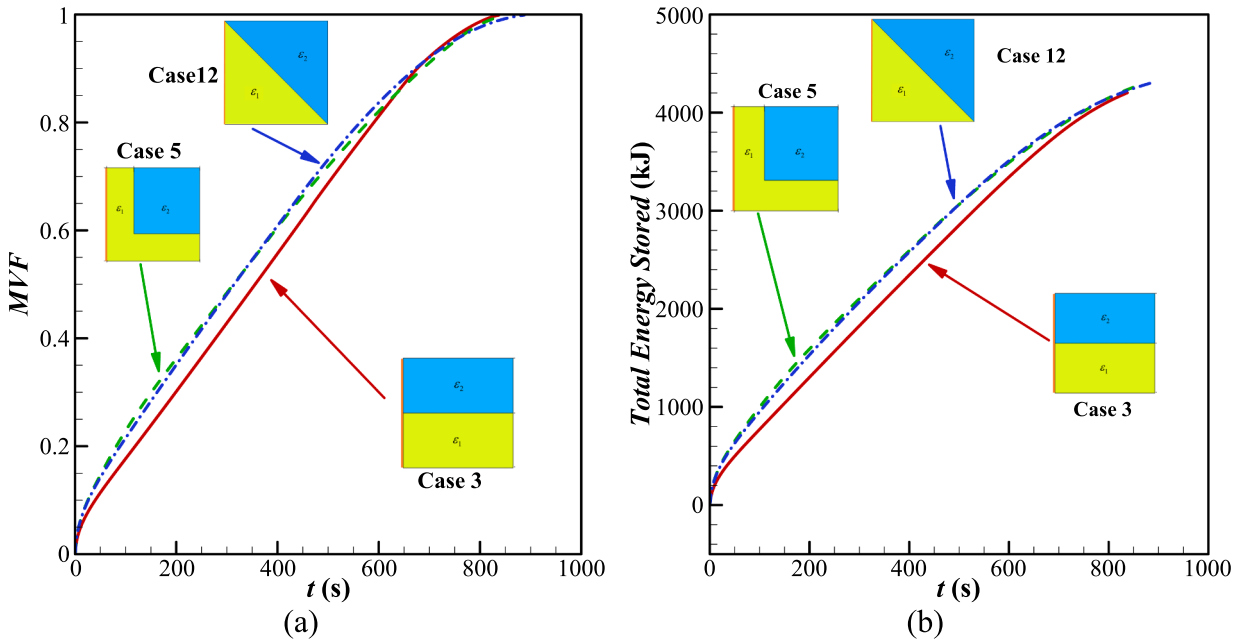

Fig. 17. The characteristics curves for best cases of groups I-III.

in Fig. 11(a). Also, the amplitude of the isotherms at the early time in case 6 is similar to that of case 8, but with increasing time, the difference in the porous arrangements in cases 6 and 8 caused case 6 to take more time to melt compared to case 8.

The melting front and flow lines in the melt area are shown for cases from 5 to 8 in Fig. 13. The flow lines are pretty distant in the first porous medium relative to the second porous medium. Also, the compaction of these lines and the lack of proper progress of the melting front in the second porous medium is evident compared to the first porous medium. The observed behavior results from the lower thermal conductivity of the second porous medium compared to the first one.

Fig. 14 depicts the MVF and total stored energy for the third group. As can be observed, the is good concordance between profiles of MVF and stored energy since the dominant form of energy storage is latent heat storage. Cases 9 and 12 show almost similar patterns, while cases 10 and 11 are also similar. The main reason for the similarity between these cases is placing the heavy foam layer next to the active wall. For cases 9 and 12 foam layer with ε_1 is located adjacent to the heated wall, while for the other two cases, the foam with porosity ε_2 is close to the heated wall. Initially, there is no molten PCM, and thus the conduction heat transfer is the dominant heat transfer mechanisms. The heavy foam layer boosts the conduction heat transfer in these cases. The best configuration among the studied cases is Case 12, with an 887 s melting time, which provides about a 32% reduction in melting time compared to case 11, with a 1226 s melting time.

Figs. 15 and 16 show the isotherms and streamlines for Cases 9–12 for three timesteps of the 60 s, 360 s, and 900 s. A foam layer with low porosity (Cases 9 and 12) accelerates the melting process at the initial times. In later times when the melting front reaches the foam with higher porosity ($\varepsilon_2 = 0.975$), the molten liquid can more freely flow in the second region. However, placing the foam with high porosity at the top is even more advantageous since it effectively contributes to the natural convection flows at the top and right region of the LHTES.

Regarding cases 10 and 11, the melting starts with a fair slope but is much smaller than in the previous cases (9 and 12). The reason is the high porosity of the foam layer next to the heated wall. Since the porosity is high, there is a larger amount of PCM in this region, while the MFPCM thermal conductivity is also low. As a result, the melting front progress slowly in this configuration. Later, when the melting front reaches the first foam layer (ε_1), it resists natural convection due to low permeability. However, it contributes to heat transfer by a better conduction heat transfer (higher composite thermal conductivity) and also a smaller amount of PCM in the pores (lower latent heat to be absorbed). Therefore, the slope of MVF and stored energy remains almost the same. Moreover, since the natural convection is weak in the first porous layer (ε_1), there is not much difference between its configuration in cases 10 and 11.

Fig. 17 compares MVF and stored energy for the best cases of each configuration. The best case among the investigated cases was selected in terms of a faster melting process (quick thermal charging). Interestingly, cases 5 and 12 show similar melting and thermal energy storage behavior, but case 3 shows different behavior. Cases 5 and 12 benefit from a full layer of low porosity foam ($\varepsilon_1 = 0.90$) next to the heated wall, followed by a well-circulated natural convection heat transfer in a high porosity layer ($\varepsilon_2 = 0.975$). However, case 3 benefits from a partial layer of low porosity metal foam at the bottom and simultaneously a layer of high porosity foam at the top, contributing to both the conduction heat transfer and free convection. Thus, case 3 starts with fair thermal conduction due to the low porosity foam layer and proper natural circulation. As a result, a constant slope for MVF could be seen during the melting process until it reaches its full melting at 837 s.

Fig. 18 scrutinizes the effect of porosity on the *MVF* for three promising cases: 3, 5, and 12, each exhibiting minimal melting times. The presumption was made that the mean porosity within the enclosure mirrors the average porosity of the original cases. Given that the area of MF layers 1 and 2 is identical, the mean porosity is computed as $(\varepsilon_1 + \varepsilon_2)/2$. Taking into account the porosity of MF layer 1 ($\varepsilon_1 = 0.9$) and layer 2 ($\varepsilon_2 = 0.975$), the derived average porosity stands at $\varepsilon = 0.9375$. Consequently, a reference case maintaining a constant average porosity of $\varepsilon = 0.9375$ across both layers was established. In addition, another case was incorporated, characterized by $\varepsilon_1 = 0.925$ and $\varepsilon_2 = 0.95$, resulting in the same average porosity of $\varepsilon = 0.9375$.

As Fig. 18 demonstrates, the use of two metal foam layers with unequal porosity yields a shorter total melting time compared to the reference case. Notably, as seen in Fig. 18(a), the *MVF* for Case 3 with $\varepsilon_1 = 0.90$ and $\varepsilon_2 = 0.975$ initially lags behind the other two cases during the early to middle stages of the melting process. However, it eventually leads, displaying the shortest melting time due to the reduced porosity of layer 2 ($\varepsilon_2 = 0.975$), which enables an effective natural convection flow in the top layer. The reference case results in a melting time of 889 s. In

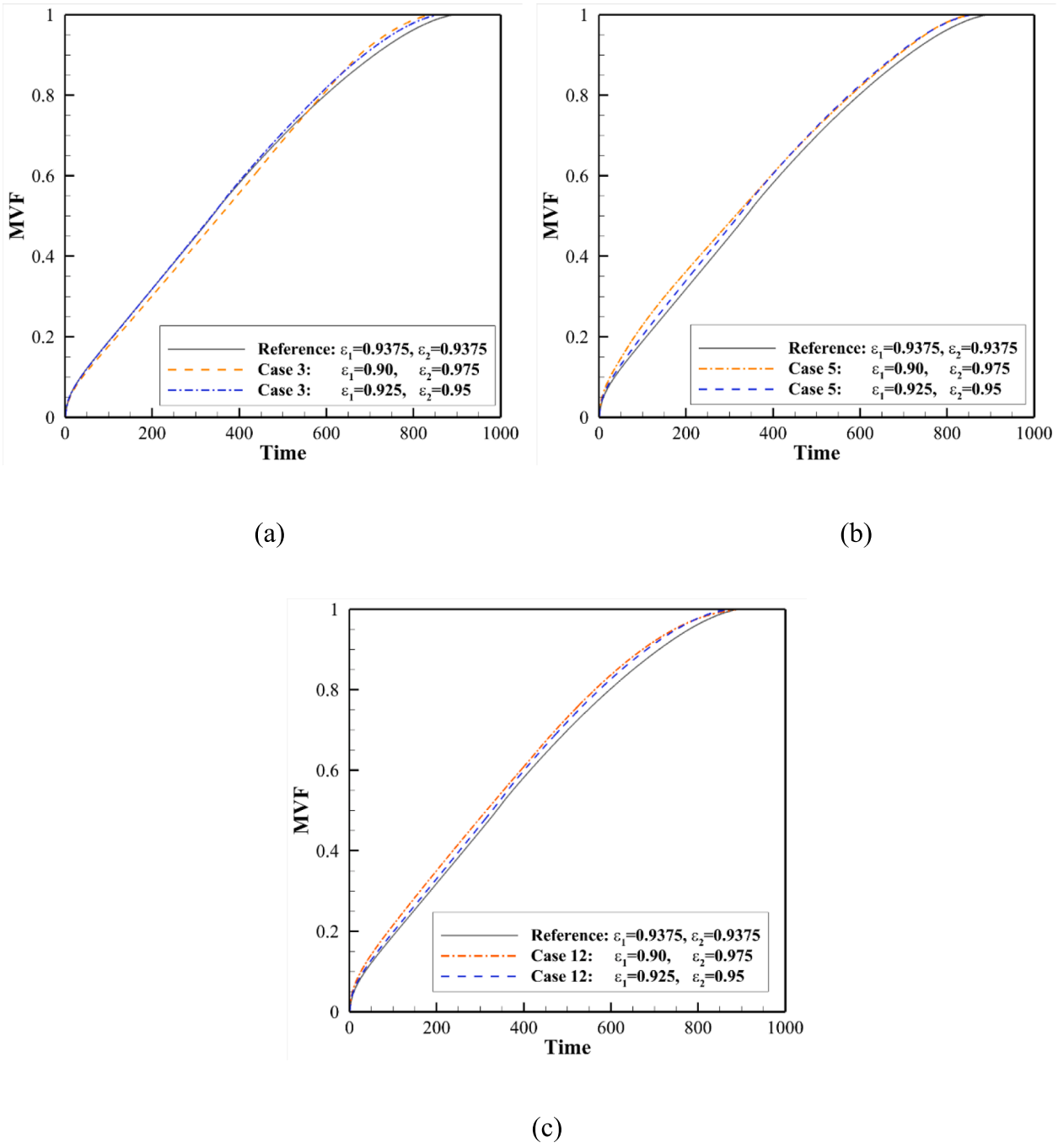

Fig. 18. The impact of porosity on the melting heat transfer for three promising design cases of 3, 5 and 12. The reference case shows the melting profile for an enclosure filled with a uniform MF of porosity 0.9375.

contrast, Case 3 with $\varepsilon_1 = 0.90$ and $\varepsilon_2 = 0.975$ records a melting time of 837 s, while Case 3 with $\varepsilon_1 = 0.925$ and $\varepsilon_2 = 0.95$ has a melting time of 854 s. Thus, Case 3 with $\varepsilon_1 = 0.90$ and $\varepsilon_2 = 0.975$ achieves approximately a 6% reduction in melting time compared to the reference. Similarly, Case 3 with $\varepsilon_1 = 0.925$ and $\varepsilon_2 = 0.95$ results in roughly 4% less melting time. Evidently, increasing the difference in porosity between layers contributes to a superior total melting time for promising design cases.

Fig. 18(b) indicates that Case 5 with $\varepsilon_1 = 0.90$ and $\varepsilon_2 = 0.975$ yields a more optimal melting profile compared to both the reference case and Case 5 with $\varepsilon_1 = 0.925$ and $\varepsilon_2 = 0.95$. The full melting time for Case 5 with $\varepsilon_1 = 0.90$ and $\varepsilon_2 = 0.975$ is approximately 5% superior to the reference case. Fig. 18(c) highlights Case 12, which exhibits the same trend of results as Case 5. The advantage of using porous layers with varying porosities becomes more apparent as the disparity in porosity between layers widens. This is primarily because a layer with higher porosity tends to enhance areas where convection dominates, while a layer with lower porosity can be beneficial in areas where heat transfer is primarily governed by conduction. This interplay between porosity and heat transfer mechanisms optimizes the melting process, thereby influencing the melting process.

5. Conclusions

The charging time of an LHTES unit with various configurations of metal foams was investigated. Two foam layers with porosities for $\varepsilon_1 =$

0.9 and $\varepsilon_2 = 0.975$ were considered heavy and light foam, respectively. A heavy foam could notably increase the effective thermal conductivity of the composite PCM and boost the conduction heat transfer mechanism. Yet, it significantly suspends the natural convection flows due to low permeability. The high porosity light foam could improve the effective thermal conductivity and allow some degrees of natural convection. Thus, a combination of these layers could boost each heat transfer mechanism where ever needed. The temperature contours and streamlines were studied to understand the physics of heat transfer enhancement better. The examined foam layer configurations were studied in three groups. In each group, four configurations were studied. Each foam layer's area (mass) was constant for all cases.

The enclosure was split in half for group I, either horizontally or vertically. The melting fraction and energy storage showed that splitting the enclosure horizontally and placing the foam layer with low thermal conductivity on top could result in the shortest thermal charging (full melting time). The shortest melting time (case 3) was 837 s, while the longest melting time was 1246 s (case 4). Therefore, changing the foam layer configuration could improve the melting time by 32%.

Regarding group II, the enclosure was divided into square and L-shape layers. Inserting a heavy layer adjacent to the heated and bottom walls, followed by the light layer at the top right corner, could boost the thermal conduction regime and allow good natural convection melting. Using this foam layer configuration could decrease the melting time by about 30% in comparison to an opposite configuration (case 6).

In group III, a diagonal division was considered for the foam layers. Placing the heavy foam (ε_1) next to the heated wall and bottom, followed by the light layer (ε_2) at the top and right (case 12), could result in the shortest melting time (887 s) for this configuration which was 391 s shorter than the opposite configuration (case 11).

A general comparison between the shortest melting time of each group shows that inserting the heavy foam layer (ε_1) adjacent to the heated and bottom walls, followed by the light foam layer next to the top and right walls, could provide the shortest melting time for each group. Moreover, among all investigated foam layer configurations, the melting time for case 3 (horizontal split with the light foam layer at the top) could provide the shortest melting time (837 s). In Case 3, the low porous layer was placed at the bottom, and the highly porous layer was placed at the top. At the same time, the low porous layer at the bottom provides an excellent, effective thermal conductivity that advances the melting process by conduction mechanism and the low porous layer at the top benefits from the free convection heat transfer circulations. Thus, overall melting process accelerates. Case 3, compared to a uniform metal foam with the same average porosity, provides a 6% shorter time.

An increase in the difference between the porosities of the MF layers leads to a decrease in melting time. This variation in porosity enhances the thermal performance of the system by optimizing the balance between convection and conduction heat transfer mechanisms, consequently speeding up the melting process.

In the present study, the impact of the metal foam configurations on the charging time was investigated. However, the discharging of PCMs is another important aspect that could be the topic of future research.

CRediT authorship contribution statement

Mohammad Ghalambaz: Conceptualization, Methodology, Writing – original draft, Software, Validation, Formal analysis, Data curation, Supervision. **Mehdi Fteiti:** Visualization, Writing – original draft, Investigation, Formal analysis, Data curation, Writing – review & editing. **Obai Younis:** Methodology, Formal analysis, Data curation, Writing – review & editing, Writing – original draft. **Mikhail Sheremet:** Investigation, Conceptualization, Methodology, Formal analysis, Writing – original draft, Writing – review & editing. **Hiba A. Hasan:** Conceptualization, Methodology, Investigation, Writing – original draft, Writing – review & editing.

Declaration of Competing Interest

The authors declare that they have no known competing financial interests or personal relationships that could have appeared to influence the work reported in this paper.

Data availability

No data was used for the research described in the article.

Acknowledgments

The authors would like to thank the Deanship of Scientific Research at Umm Al-Qura University for supporting this work by Grant Code: (23UQU4310414DSR006). This research of Mohammad Ghalambaz and Mikhail Sheremet was supported by the Tomsk State University Development Programme (Priority-2030).

References

[1] Y. Filali Baba, H. Ajdad, A.A.L. Mers, Y. Grosu, A. Faik, Multilevel comparison between magnetite and quartzite as thermocline energy storage materials, Appl. Therm. Eng. 149 (2019) 1142–1153.
[2] Z. Badiei, M. Eslami, K. Jafarpur, Performance improvements in solar flat plate collectors by integrating with phase change materials and fins: A CFD modeling, Energy 192 (2020).
[3] A. Mawire, C.S. Ekwomadu, T.M. Lefenya, A. Shobo, Performance comparison of two metallic eutectic solder based medium-temperature domestic thermal energy storage systems, Energy 194 (2020).
[4] S.S. Mostafavi Tehrani, Y. Shoraka, K. Nithyanandam, R.A. Taylor, Shell-and-tube or packed bed thermal energy storage systems integrated with a concentrated solar power: A techno-economic comparison of sensible and latent heat systems, Appl. Energy 238 (2019) 887–910.
[5] A. Saxena, P. Verma, G. Srivastava, N. Kishore, Design and thermal performance evaluation of an air heater with low cost thermal energy storage, Appl. Therm. Eng. 167 (2020).
[6] M. Dardir, K. Panchabikesan, F. Haghighat, M. El Mankibi, Y. Yuan, Opportunities and challenges of PCM-to-air heat exchangers (PAHXs) for building free cooling applications—A comprehensive review, J. Storage Mater. 22 (2019) 157–175.
[7] A.R. Shaibani, M.M. Keshtkar, P. Talebizadeh Sardari, Thermo-economic analysis of a cold storage system in full and partial modes with two different scenarios: A case study, J. Storage Mater. 24 (2019).
[8] L. Qiu, Y. Ouyang, Y. Feng, X. Zhang, Review on micro/nano phase change materials for solar thermal applications, Renew. Energy 140 (2019) 513–538.
[9] X.-Y. Li, L. Yang, X.-L. Wang, X.-Y. Miao, Y. Yao, Q.-Q. Qiang, Investigation on the charging process of a multi-PCM latent heat thermal energy storage unit for use in conventional air-conditioning systems, Energy 150 (2018) 591–600.
[10] A. Farzanehnia, M. Khatibi, M. Sardarabadi, M. Passandideh-Fard, Experimental investigation of multiwall carbon nanotube/paraffin based heat sink for electronic device thermal management, Energ. Conver. Manage. 179 (2019) 314–325.
[11] D. Luo, L. Xiang, X. Sun, L. Xie, D. Zhou, S. Qin, Phase-change smart lines based on paraffin-expanded graphite/polypropylene hollow fiber membrane composite phase change materials for heat storage, Energy 197 (2020).
[12] R.K. Sharma, P. Ganesan, V.V. Tyagi, H.S.C. Metselaar, S.C. Sandaran, Developments in organic solid–liquid phase change materials and their applications in thermal energy storage, Energ. Conver. Manage. 95 (2015) 193–228.
[13] L.F. Cabeza, A. Gutierrez, C. Barreneche, S. Ushak, Á.G. Fernández, A. Inés Fernádez, M. Grágeda, Lithium in thermal energy storage: A state-of-the-art review, Renew. Sustain. Energy Rev. 42 (2015) 1106–1112.
[14] Z.-Q. Zhu, Y.-K. Huang, N. Hu, Y. Zeng, L.-W. Fan, Transient performance of a PCM-based heat sink with a partially filled metal foam: Effects of the filling height ratio, Appl. Therm. Eng. 128 (2018) 966–972.
[15] A. Gil, M. Medrano, I. Martorell, A. Lázaro, P. Dolado, B. Zalba, L.F. Cabeza, State of the art on high temperature thermal energy storage for power generation. Part 1—Concepts, materials and modellization, Renew. Sustain. Energy Rev. 14 (2010) 31–55.
[16] S. Zhang, D. Feng, L. Shi, L. Wang, Y. Jin, L. Tian, Z. Li, G. Wang, L. Zhao, Y. Yan, A review of phase change heat transfer in shape-stabilized phase change materials (ss-PCMs) based on porous supports for thermal energy storage, Renew. Sustain. Energy Rev. 135 (2021).
[17] F. Li, X. Huang, Y. Li, L. Lu, X. Meng, X. Yang, B. Sundén, Application and analysis of flip mechanism in the melting process of a triplex-tube latent heat energy storage unit, Energy Rep. 9 (2023) 3989–4004.
[18] R. Tauseef ur, H.M. Ali, M.M. Janjua, U. Sajjad, W.-M. Yan, A critical review on heat transfer augmentation of phase change materials embedded with porous materials/foams, Int. J. Heat Mass Transfer, 135 (2019) 649-673.
[19] P.T. Sardari, D. Grant, D. Giddings, G.S. Walker, M. Gillott, Composite metal foam/PCM energy store design for dwelling space air heating, Energ. Conver. Manage. 201 (2019).

[20] B. Buonomo, H. Celik, D. Ercole, O. Manca, M. Mobedi, Numerical study on latent thermal energy storage systems with aluminum foam in local thermal equilibrium, Appl. Therm. Eng. 159 (2019).
[21] A. Pourakabar, A.A. Rabienataj Darzi, Enhancement of phase change rate of PCM in cylindrical thermal energy storage, Appl. Therm. Eng. 150 (2019) 132–142.
[22] P.T. Sardari, H.I. Mohammed, D. Giddings, G.S. walker, M. Gillott, D. Grant, Numerical study of a multiple-segment metal foam-PCM latent heat storage unit: Effect of porosity, pore density and location of heat source, Energy, 189 (2019).
[23] X. Yang, Z. Guo, Y. Liu, L. Jin, Y.-L. He, Effect of inclination on the thermal response of composite phase change materials for thermal energy storage, Appl. Energy 238 (2019) 22–33.
[24] M.M. El Idi, M. Karkri, Heating and cooling conditions effects on the kinetic of phase change of PCM embedded in metal foam, Case Stud. Therm. Eng. 21 (2020).
[25] E.I. Mohamed Moussa, M. Karkri, A numerical investigation of the effects of metal foam characteristics and heating/cooling conditions on the phase change kinetic of phase change materials embedded in metal foam, J. Storage Mater. 26 (2019).
[26] Z. Wang, J. Wu, D. Lei, H. Liu, J. Li, Z. Wu, Experimental study on latent thermal energy storage system with gradient porosity copper foam for mid-temperature solar energy application, Appl. Energy 261 (2020).
[27] R.P. Singh, H. Xu, S.C. Kaushik, D. Rakshit, A. Romagnoli, Charging performance evaluation of finned conical thermal storage system encapsulated with nano-enhanced phase change material, Appl. Therm. Eng. 151 (2019) 176–190.
[28] J.M. Mahdi, H.I. Mohammed, E.T. Hashim, P. Talebizadehsardari, E.C. Nsofor, Solidification enhancement with multiple PCMs, cascaded metal foam and nanoparticles in the shell-and-tube energy storage system, Appl. Energy 257 (2020).
[29] C. Nie, J. Liu, S. Deng, Effect of geometry modification on the thermal response of composite metal foam/phase change material for thermal energy storage, Int. J. Heat Mass Transf. 165 (2021).
[30] N. Bianco, M. Iasiello, G.M. Mauro, L. Pagano, Multi-objective optimization of finned metal foam heat sinks: Tradeoff between heat transfer and pressure drop, Appl. Therm. Eng. 182 (2021).
[31] Y. Huang, Q. Sun, F. Yao, C. Zhang, Experimental Study on the Thermal Performance of a Finned Metal Foam Heat Sink with Phase Change Material, Heat Transfer Eng. 42 (2020) 579–591.
[32] Z.A. Qureshi, E. Elnajjar, O. Al-Ketan, R.A. Al-Rub, S.B. Al-Omari, Heat transfer performance of a finned metal foam-phase change material (FMF-PCM) system incorporating triply periodic minimal surfaces (TPMS), Int. J. Heat Mass Transf. 170 (2021).
[33] W.Q. Li, S.J. Guo, L. Tan, L.L. Liu, W. Ao, Heat transfer enhancement of nano-encapsulated phase change material (NEPCM) using metal foam for thermal energy storage, Int. J. Heat Mass Transf. 166 (2021).
[34] M. Hassani Soukht Abandani, D. Domiri Ganji, Melting effect in triplex-tube thermal energy storage system using multiple PCMs-porous metal foam combination, J. Energy Storage, 43 (2021).
[35] J. Sutradhar, R. Kothari, S.K. Sahu, Melting and solidification analysis of phase change material-metal foam composite with expansion/shrinkage void in rectangular system, J. Storage Mater. 47 (2022).
[36] X.K. Yu, Y.B. Tao, Y. He, Z.C. Lv, Temperature control performance of high thermal conductivity metal foam/paraffin composite phase change material: An experimental study, J. Storage Mater. 46 (2022).
[37] Y. Zhuang, J. Lin, A. Liu, Numerical investigation on non-Newtonian melting heat transfer of phase change material composited with nanoparticles and metal foam in an inner heated cubic cavity, J. Storage Mater. 51 (2022).
[38] C. Naldi, M. Dongellini, G.L. Morini, The evaluation of the effective thermal conductivity of metal-foam loaded phase change materials, J. Storage Mater. 51 (2022).
[39] H. Shakibi, S. Afzal, A. Shokri, B. Sobhani, Utilization of a phase change material with metal foam for the performance improvement of the photovoltaic cells, J. Storage Mater. 51 (2022).
[40] J.S. Baruah, V. Athawale, P. Rath, A. Bhattacharya, Melting and energy storage characteristics of macro-encapsulated PCM-metal foam system, Int. J. Heat Mass Transf. 182 (2022).
[41] S. Huang, J. Lu, Y. Li, Numerical study on the influence of inclination angle on the melting behaviour of metal foam-PCM latent heat storage units, Energy 239 (2022).
[42] H.M. Ali, Heat transfer augmentation of porous media (metallic foam) and phase change material based heat sink with variable heat generations: An experimental evaluation, Sustainable Energy Technol. Assess. 52 (2022).
[43] Z. Du, G. Liu, X. Huang, T. Xiao, X. Yang, Y.-L. He, Numerical studies on a fin-foam composite structure towards improving melting phase change, Int. J. Heat Mass Transf. 208 (2023), 124076.
[44] A.A. Nnanna, A. Haji-Sheikh, K.T. Harris, Experimental study of local thermal non-equilibrium phenomena during phase change in porous media, Int. J. Heat Mass Transf. 47 (2004) 4365–4375.
[45] K. Jiao, L. Lu, T. Wen, Q. Wang, A modified mixture theory for one-dimensional melting of pure PCM and PCM/metal foam composite: numerical analysis and experiment validation, Int. J. Heat Mass Transf. 186 (2022), 122461.
[46] X. Hu, X. Gong, Pore-scale numerical simulation of the thermal performance for phase change material embedded in metal foam with cubic periodic cell structure, Appl. Therm. Eng. 151 (2019) 231–239.
[47] J.M. Mahdi, H.I. Mohammed, E.T. Hashim, P. Talebizadehsardari, E.C. Nsofor, Solidification enhancement with multiple PCMs, cascaded metal foam and nanoparticles in the shell-and-tube energy storage system, Appl. Energy 257 (2020), 113993.
[48] H. Zuo, M. Wu, K. Zeng, Y. Zhou, J. Kong, Y. Qiu, M. Lin, G. Flamant, Numerical investigation and optimal design of partially filled sectorial metal foam configuration in horizontal latent heat storage unit, Energy 237 (2021), 121640.
[49] S.M.H. Zadeh, S. Mehryan, M. Ghalambaz, M. Ghodrat, J. Young, A. Chamkha, Hybrid thermal performance enhancement of a circular latent heat storage system by utilizing partially filled copper foam and Cu/GO nano-additives, Energy 213 (2020), 118761.
[50] H. Zheng, C. Wang, Q. Liu, Z. Tian, X. Fan, Thermal performance of copper foam/paraffin composite phase change material, Energ. Conver. Manage. 157 (2018) 372–381.
[51] A. Bhattacharya, V.V. Calmidi, R.L. Mahajan, Thermophysical properties of high porosity metal foams, Int. J. Heat Mass Transf. 45 (2002) 1017–1031.
[52] X. Xiao, P. Zhang, M. Li, Preparation and thermal characterization of paraffin/metal foam composite phase change material, Appl. Energy 112 (2013) 1357–1366.
[53] D.A. Nield, A. Bejan, Convection in porous media, Springer, 2006.
[54] O.C. Zienkiewicz, R.L. Taylor, P. Nithiarasu, The Finite Element Method for Fluid Dynamics, Seventh, Edition ed., Butterworth-Heinemann, Oxford, 2014.
[55] G. Söderlind, L. Wang, Adaptive time-stepping and computational stability, J. Comput. Appl. Math. 185 (2006) 225–243.
[56] C. Gau, R. Viskanta, Melting and solidification of a pure metal on a vertical wall, (1986).
[57] A. Brent, V.R. Voller, K. Reid, Enthalpy-porosity technique for modeling convection-diffusion phase change: application to the melting of a pure metal, Numer. Heat Transfer Part A Appl. 13 (1988) 297–318.